- 1 Molecular architecture of 40S initiation complexes on the Hepatitis C virus
- 2 IRES: from ribosomal attachment to eIF5B-mediated reorientation of initiator
- 3 tRNA
- 4 Author List and Affiliations
- 5 Zuben P. Brown¹, Irina S. Abaeva², Swastik De¹, Christopher U.T. Hellen², Tatyana V. Pestova^{*2},
- 6 and Joachim Frank $*^{1,3}$.
- ⁷ ¹Department of Biochemistry and Molecular Biophysics, Columbia University, New York, NY,
- 8 USA
- 9 ²Department of Cell Biology, SUNY Downstate Health Sciences University, Brooklyn, NY, USA
- ³Department of Biological Sciences, Columbia University, New York, NY, USA
- 11 *Authors for correspondence (Tatyana.Pestova@downstate.edu; jf2192@cumc.columbia.edu)
- 12 Lead Contact: Joachim Frank*^{1,3}
- 13
- 14
- 15
- 10
- 16

17

18 SUMMARY

19

20 Hepatitis C virus mRNA contains an internal ribosome entry site (IRES) that mediates end-independent 21 translation initiation, requiring a subset of eukaryotic initiation factors (eIFs). Direct binding of the IRES 22 to the 40S subunit places the initiation codon into the P site, where it base-pairs with eIF2-bound Met-23 tRNA^{Met} forming a 48S initiation complex. Then, eIF5 and eIF5B mediate subunit joining. Initiation can also proceed without eIF2, in which case Met-tRNA_i^{Met} is recruited directly by eIF5B. Here, we present 24 25 cryo-EM structures of IRES initiation complexes at resolutions up to 3.5 Å that cover all major stages from 26 initial ribosomal association, through eIF2-containing 48S initiation complexes, to eIF5B-containing 27 complexes immediately prior to subunit joining. These structures provide insights into the dynamic network 28 of 40S/IRES contacts, highlight the role for IRES domain II, and reveal conformational changes that occur 29 during the transition from eIF2- to eIF5B-containing 48S complexes that prepare them for subunit joining. 30

31 Keywords

32 hepatitis C virus IRES, ribosome, eIF2, eIF5B, translation initiation, cryo-EM

33 INTRODUCTION

34 The canonical initiation process begins with formation of the 43S preinitiation complex (PIC) comprising the 40S ribosomal subunit, the eIF2•GTP/Met-tRNA_i^{Met} ternary complex (eIF2-35 36 TC), eIF1, eIF1A and eIF3 (Jackson et al., 2010). The 43S PIC attaches to the capped 5'-terminal 37 region of mRNA and then scans to the initiation codon in a favorable nucleotide context 38 (containing A/G and G at the -3 and +4 positions relative to the AUG, respectively) where it stops 39 and forms the 48S initiation complex (IC) with established codon-anticodon base-pairing. 40 Attachment is mediated by eIFs 4A, 4B and eIF4F, which cooperatively unwind the cap-proximal 41 region allowing attachment and also assist 43S PIC scanning. eIF1, in cooperation with eIF1A, 42 induces an 'open' scanning-competent conformation of the 43S PIC and monitors the fidelity of 43 initiation codon selection (Pestova et al., 1998a; Pestova and Kolupaeva, 2002; Passmore et al., 44 2007; Hussain et al., 2014). Establishment of codon-anticodon base-pairing in the 48S IC leads to 45 dissociation of eIF1 and eIF5-induced hydrolysis of eIF2-bound GTP, and thereby switches the 46 40S subunit to the 'closed' conformation (Unbehaun et al., 2004; Maag et al., 2005). After that, eIF5B, in its GTP-bound form, displaces residual eIF2•GDP (Pisarev et al., 2006) and promotes 47 joining of the 60S subunit (Pestova et al., 2000). Interaction of eIF5B with eIF1A enhances 48 49 eIF5B's subunit joining activity and the hydrolysis of eIF5B-bound GTP, leading to coupled 50 release of eIF5B•GDP and eIF1A from the assembled 80S ribosome (Marintchev et al., 2003; 51 Acker et al., 2006; Nag et al., 2016).

52 A number of viral mRNAs contain internal ribosomal entry sites (IRESs), structured RNA regions that mediate cap-independent initiation of translation using a subset of the eIFs that are 53 54 required by canonical initiation. All IRES-mediated initiation mechanisms are based on non-55 canonical interactions of IRESs with canonical components of the translation apparatus (Jackson 56 et al, 2010). The ~300nt-long hepatitis C virus (HCV) IRES is located in the 5'-terminal region of 57 the viral genome and epitomizes a class of related RNA elements. HCV-like IRESs occur in the 58 genomes of pestiviruses (e.g., classical swine fever virus (CSFV)), some pegiviruses and numerous 59 members of Picornaviridae (Arhab et al., 2020). The HCV IRES comprises three domains (II-IV), with domain III divided into several subdomains (Figure 1A). Ribosomal recruitment of HCV 60 61 and HCV-like IRESs occurs by direct binding of the IRES to the 40S subunit and does not involve scanning, group 4 eIFs or eIF1 (Pestova et al., 1998b). Domain III binds at the back of the 40S 62 63 subunit, whereas the long, bent domain II loops out and reaches into the E site. The sites of

64 interaction with the 40S subunit include domains IIIa and IIIc (which bind to eS1, eS26 and eS27), 65 the apex of domain IIId (which base-pairs to expansion segment (ES) 7 of 18S rRNA), domain 66 IIIe (which interacts with helix (h) 26 of 18S rRNA), and the apex of domain II, which interacts 67 with uS7 and eS25 in the head and uS11 on the platform of the 40S subunit, intercalating into the 68 mRNA binding channel and causing tilting of the head and forcing the 40S subunit to adopt the 69 open conformation (Kolupaeva et al., 2000; Kieft et al., 2001; Malygin et al., 2013a; 2013b; 70 Hashem et al., 2013; Angulo et al., 2016; Matsuda and Mauro, 2014; Quade et al., 2015; 71 Yamamoto et al., 2015; Yokoyama et al., 2019).

72 Although domain II does not contribute to the affinity of the HCV IRES to the 40S subunit (e.g. Kieft et al., 2001; Spahn et al., 2001), the open conformation of the 40S subunit promoted by 73 74 domain II facilitates loading of the region containing the initiation codon into the mRNA binding 75 channel, accounting for the stimulatory role of domain II during initiation on HCV-like IRESs 76 (Honda et al., 1996; Reynolds et al., 1996; Filbin and Kieft, 2011; Odreman-Macchioli et al., 77 2001). Upon binding to the 40S subunit, domain IV of the HCV IRES unfolds, and the initiation 78 codon is placed in the immediate vicinity of the P site, where it base-pairs with the anticodon of Met-tRNA^{iMet} as a part of the eIF2-TC, leading to formation of the 48S IC (Pestova et al., 1998b). 79 80 After that, eIF5 and eIF5B mediate the subunit joining step to complete formation of the 81 elongation-competent 80S ribosome (Locker et al., 2007; Pestova et al., 2008; Terenin et al., 2008). Notably, in 80S complexes assembled on the HCV IRES, the P-site Met-tRNA^{Met} and eIF5B•GTP. 82 83 which correspond to the last stage in the initiation process prior to formation of an elongation-84 competent ribosome, the tilt of the 40S subunit is reversed, and the apex of domain II is released 85 from its position on the head of the 40S subunit (Yamamoto et al., 2014). Remarkably, when levels of active eIF2 are reduced due to stress-induced phosphorylation, Met-tRNA_i^{Met} can be recruited 86 87 by eIF5B instead to the IRES/40S complexes (Pestova et al., 2008; Terenin et al., 2008). In both 88 eIF2- and eIF5B-mediated pathways, eIF1A enhances 48S complex formation (de Breyne et al., 89 2008; Jaafar et al., 2016), whereas eIF1 inhibits the process and even induces dissociation of preassembled 48S ICs, but this inhibition can be alleviated by deletion of domain II (Pestova et al., 90 91 2008).

In addition to 40S subunits, HCV and related IRESs also bind to eIF3 via their apical IIIa
and IIIb domains (Pestova et al., 1998b; Sizova et al., 1998; Ji et al., 2004; Hashem et al., 2013).
Strikingly, in 40S/IRES/eIF3 complexes, HCV-like IRESs displace eIF3 from its ribosomal

95 position (Hashem et al., 2013), usurping eIF3's key ribosomal contacts involving eS1, eS26 and 96 eS27 (des Georges et al., 2015). Moreover, the ribosome-binding surface of eIF3 is now involved 97 in interaction with the IRES (Hashem et al., 2013). In in vitro reconstituted initiation reactions, 98 eIF3 only modestly enhances 48S complex formation on HCV-like IRESs (Pestova et al., 1998b; 99 Hashem et al., 2013), which led to the suggestion that in vivo, the role of the eIF3/IRES interaction 100 is likely to relieve the competition between the IRES and eIF3 for a common ribosomal binding 101 site, and to reduce formation of 43S PICs, thereby favoring translation of viral mRNAs (Hashem 102 et al., 2013).

103 Cryo-EM studies have been indispensable in providing insights into the architecture and 104 interactions of HCV and HCV-like IRES ribosomal complexes, as well as the mechanism of the 105 IRES function, initially through low-resolution 40S/HCV IRES and 80S/HCV IRES structures 106 (Spahn et al. 2001; Boehringer et al, 2005) and continuing with sub-nanometer resolution 107 structures of 40S/eIF3/CSFV IRES and 80S/Met-tRNA;^{Met}/eIF5B•GMPPNP/HCV IRES 108 functional complexes (Hashem et al., 2013; Yamamoto et al., 2014), and the more recent near-109 atomic resolution reconstructions of 80S•HCV IRES complexes (Yamamoto et al., 2015; Quade 110 et al., 2015; Yokoyama et al., 2019). However, despite these advances, the structures of 48S ICs 111 assembled on the HCV IRES, as well as the transitions between different states in the initiation 112 pathways and accompanying conformational changes have remained unknown. To fill these gaps, 113 we present cryo-EM structures of HCV IRES ribosomal complexes up to 3.5 Å resolution that 114 cover all major stages of IRES-mediated initiation pathways from IRES binding to the 40S subunit 115 through eIF2-containing 48S ICs to the final eIF5B-containing 48S ICs immediately prior to the 116 joining of the 60S subunit. Individually, these structures also provide detailed insights into the 117 dynamic network of contacts between the IRES and the 40S subunit, highlight the role for IRES 118 domain II, and importantly, include the first structure of eIF5B bound to the 40S subunit, prior to 119 subunit joining.

- 120
- 121
- 122
- 123
- 124
- 125

126 **RESULTS AND DISCUSSION**

127

128 Overview of cryo-EM analysis of initiation complexes assembled on the wt and the ΔdII HCV 129 IRES with eIF2 or eIF5B

130 To capture discrete states within either the eIF2- or eIF5B-containing IRES-mediated 131 initiation pathways and to visualize the role of IRES domain II in these processes, initiation 132 complexes were assembled *in vitro* by incubating the *wt* or the Δ dII mutant IRES (Figure 1A) with 133 individual purified translation components. To follow the eIF2-mediated pathway, reaction 134 mixtures were prepared containing the wt or the ΔdII IRES, 40S ribosomal subunits, eIF2, eIF3, 135 eIF1A and Met-tRNA^{iMet}, and to follow the eIF5B-mediated pathway, eIF2 was replaced by eIF5B, 136 thus yielding four discrete sample types (Table S1). Cryo-EM grids of each complex were imaged 137 at 300 kV producing high-contrast micrographs with easily identifiable 40S ribosomal particles 138 (Figure S1A-E; Table S2). The images were processed using maximum-likelihood classification 139 techniques implemented in Relion 3.1 (Scheres, 2012; 2016; Zivanov et al., 2018; 2019) yielding 18 structures containing different sets of components at resolutions as high as 3.5 Å (Figure S2; 140 141 Table S3). Although some flexible regions had a poor local resolution (e.g., eS12 in the 40S head 142 or IRES domain IIIb), most of the ribosome, all IRES-ribosome contacts, and all initiation factors 143 present had resolutions, between 3-7 Å (Figures S2 and S3), that allowed modeling of all these 144 components. None of the structures obtained contained eIF3. During initiation on HCV-like 145 IRESs, eIF3 interacts with the apical region of IRES domain III rather than with the 40S subunit 146 (Hashem et al., 2013). This interaction is sensitive to the process of grid preparation and is more 147 stable when grids have thicker ice so that imaging complexes that contain eIF3 requires the 148 intentional selection of regions with sufficiently thick ice (e.g., Hashem at al., 2013; Neupane et al., 2020); however, our study aimed to determine the details of ribosomal interactions with the 149 150 IRES, initiation factors and Met-tRNA_i^{Met} at high resolution, which relies on imaging in regions 151 with thinner ice. Importantly, however, the absence of eIF3 does not affect data interpretation 152 because all studied complexes can be assembled efficiently without eIF3 (Pestova et al., 1998b; 153 2008).

154 The structures obtained comprise the $40S/IRES_{\Delta dII}$ binary complex in various 155 conformational states (structures $1_{\Delta dII}-9_{\Delta dII}$); the $40S/IRES_{wt}$ binary complex in a single 156 conformational state (structure 10_{wt}); the $40S/eIF1A/IRES_{wt}$ ternary complex (structure 11_{wt}); 48S

5

157 ICs containing eIF2, Met-tRNA_i^{Met}, eIF1A and the *wt* or the Δ dII IRES (structures 12_{wt} and 12_{Δ dII}); 158 48S complexes containing the *wt* or the Δ dII IRES base-paired with the P-site Met-tRNA_i^{Met} but 159 lacking eIF2 and thus mimicking the stage after eIF2 dissociation following hydrolysis of GTP 160 (structures 13_{wt} and 13_{Δ dII}); the pre-48S IC containing eIF5B, eIF1A, the *wt* IRES and P-site Met-161 tRNA_i^{Met} that is not base-paired with the initiation codon (structure 14_{wt}); and 48S ICs containing 162 eIF5B, eIF1A, Met-tRNA_i^{Met} and the *wt* or the Δ dII IRES (structures 15_{wt} and 15_{Δ dII}) (Figure 1B). 163 Thus, the structures obtained cover the entire initiation pathway, starting with initial

binding of the IRES to the 40S subunit and finishing with the eIF5B-containing 48S complex prior to subunit joining, and also provide details of the dynamic interactions between the IRES and the 40S subunit (Figures 1C and S4; Table S4).

167

168 Stepwise binding of the IRES to the 40S subunit

169 Binding of the IRES to the 40S subunit involves multiple contacts formed by several IRES 170 domains (IIIa, IIIc, IIId, IIIe, S2) and ribosomal proteins eS1, eS27, eS28 as well as h26 in ES7 of 171 18S rRNA (e.g., Ouade et al., 2015; Yamamoto et al., 2015). Deletion or mutation of these domains impairs binding of the IRES to the 40S subunit to different extents, reflecting their cumulative 172 173 importance for IRES function (Kieft et al., 2001). Strikingly, classification of ribosomal complexes 174 formed on the AdII IRES identified a small proportion of 40S/IRES binary complexes that showed 175 conformational differences in the individual positions of IRES domains IIIa/IIIc/IIId/IIIe/IIIf 176 (structures $1_{\Delta dII}$ - $6_{\Delta dII}$) compared to other complexes, in all of which these domains had similar 177 positions (structures $7_{\Delta dII}$ -15_{wt/\DeltadII}) (Figure 1B). The local resolution of the IRES contacts with the 178 40S subunit in these maps was sufficient for model building of all components (Figures S2 and 179 S3) and allowed detailed examination of the relative motion of the Δ dII IRES as it transitioned 180 from a minimally associated state (structure $1_{\Delta dII}$) to the canonically bound conformation in which 181 domains IIIa, IIIc, IIId, and IIIe contact eS1, eS27 and h26 (structure $6_{\Delta dII}$ and structures $7_{\Delta dII}$ -182 $15_{wt/\Delta dII}$).

By ordering these structures based on the number of IRES-40S subunit contacts and displacement from the canonically-bound IRES position we produced a putative sequence of binding events between the Δ dII IRES and the 40S subunit (Figure 2A; Table S4). Comparison between the least- and the most- bound states (structures $1_{\Delta dII}$ and $6_{\Delta dII}$) shows that the IRES domains undergo displacement of varying extents during IRES binding (Figure 2B). Across all

188 structures, the most uniform regions of the IRES are the linked domains IIIa and IIIc (Figures 2A-189 B), which contact eS27 via nt. 163 and 233 as reported (Quade et al., 2015; Yamamoto et al., 190 2015). Given that these domains undergo minimal structural change regardless of the conformation 191 of the rest of the IRES, the observed impairment of IRES activity by nucleotide substitutions (e.g., 192 Tang et al., 1999) suggests that these interactions are critical for correct IRES function. Other IRES 193 domains, however, are more dynamic. Thus, to transition from the least- to the most-bound states requires translation of domain IIId by 10.6 Å toward the intersubunit face and domains 194 hIII₁/IIIe/IIIf by 23.3 Å toward the mRNA exit channel, whereas domains IIIa/IIIc only move by 195 196 5.9 Å (Figure 2B).

197 The fully bound IRES forms Watson-Crick base pairs between ES7 nt U₁₁₁₄₋₁₁₁₈ and IRES 198 domains IIId (GGG₂₆₆₋₂₆₈), IIIe (A₂₉₆), and hIII₁ (A₁₃₆) as well as a stacking interaction between 199 domain IIIe (G₂₉₅) and U₁₁₁₅ of ES7 (Quade et al., 2015; Yamamoto et al., 2015). This network of 200 interactions also occurred in the later-stage complexes (structures $6_{\Delta dII}$ and $7_{\Delta dII}$ -15_{wt/\Delta dI}) but they were not present during early-stage association of the IRES with the 40S subunit (structure $1_{\Delta dII}$) 201 202 (Figure 2C; summarized in Figure S4 and Table S4). Initially, the only contact between the IRES 203 and ES7 is a transient and previously undescribed stacking pair between G₂₉₆ in domain IIIe and 204 U_{1115} of 18S rRNA. Structure $1_{\Delta dII}$ also shows another transient, previously undescribed hydrogen 205 bond between U₂₆₅ in domain IIId and Lys199 in eS1, a residue that instead interacts with IIIe in 206 the fully bound IRES (Quade et al., 2015; Yamamoto et al., 2015). These two contacts along with 207 the domain IIIa/IIIc interactions with eS27 are the only bonds between the IRES and the 40S 208 subunit in this complex (Table S4). In structure $2_{\Delta dII}$, domain IIId begins to be repositioned, moving by 4.4 Å relative to structure $1_{\Delta dII}$, and the transient domain IIIe-U₁₁₁₅ contacts are lost. Although 209 210 the full complement of interactions with ES7 is not present, the Watson-Crick base-pairs between 211 domain IIId (GG₂₆₆₋₂₆₇) and CC₁₁₁₇₋₁₁₁₈ and stacking interactions of G₂₉₅ and A₂₉₆ in domain IIIe 212 with ES7 have formed. These Watson-Crick base pairs and the G₂₉₅ stacking interaction are 213 maintained in all subsequent (structures $2_{\Delta dII}$ - $6_{\Delta dII}$) and fully bound complexes (structures $7_{\Delta dII}$ -214 $15_{wt/\Delta dI}$), but the A₂₉₆ stacking interaction with U₁₁₁₅ is only present for this and the following 215 complex (structures $2_{\Delta dII}$ and $3_{\Delta dII}$). Another interaction that first appears in structure $2_{\Delta dII}$ is the eS27 216 Glu75 hydrogen bond with domain IIId nts. 266-267. It is maintained in all subsequent structures 217 except those that have domain II inserted into the E site of the 40S subunit (structures 10_{wt}, 11_{wt} 218 and 14_{wt} ; Table S4). In the following complex (structure $3_{\Delta dII}$), domain IIId is located closer to the

219 platform of the 40S subunit, moving by 2.8 Å; the S1/S2/hIII₁/IIIe/IIIf region moves by 5.0 Å, 220 whereas the position of the stable domain IIIa/IIIc changes by only 1.5 Å. This repositioning breaks 221 none of the contacts formed in structure $2_{\Delta dII}$ and allows the formation of a new base-pair between 222 G₂₆₈ in domain IIId and C₁₁₁₆ in ES7. The IRES domains continue to move closer to their canonical 223 bound positions in structure $4_{\Delta dII}$, which lacks the transient A₂₉₆/U₁₁₁₅ interaction but maintains all 224 other ribosomal contacts (Table S4). In structures $5_{\Delta dII}$ and $6_{\Delta dII}$, the final canonical interactions of 225 hIII₁ (A₁₃₆) and domain IIIe (A₂₉₆) with ES7 are present. The contact between A₁₃₆ and U₁₁₁₅ is 226 enabled because the base pairing between domain IIIe U₂₉₇ and A₂₈₈ in hIII₁ that induces the 227 flipping-out of A₁₃₆ exists in all structures ($1_{\Delta dII}$ - $15_{wt/\Delta dII}$) (Easton et al., 2009). Structures $5_{\Delta dII}$ and 228 6_{AdII} are also the first complexes in which the IRES is in a position to form a hydrogen bond between 229 Asn147 in eS1 and the phosphate backbone of GG₃₀₀₋₃₀₁, an interaction that is maintained 230 throughout all subsequent complexes (Table S4).

Taken together, this series of structures $(1_{\Delta dII}-6_{\Delta dII})$ indicates a likely sequence of binding events between the 40S subunit and the IRES from initial encounter to the canonically-bound conformation in which domain IIIa/IIIc, the first element of the IRES to bind to the 40S subunit, acts as a pivot to dock domain IIId onto ES7. These structures may represent transient states in binding of both the Δ dII and *wt* IRES, which we were able to capture in the former case because the altered kinetic landscape of the initiation pathway in the absence of domain II allowed them to accumulate and be observed.

238 An important corollary of IRES binding is the conformational changes that occur in the 40S subunit. Whereas complexes with an incompletely accommodated IRES (structures $1_{\Delta dII}$ - $5_{\Delta dII}$) 239 240 contain 40S subunits in the analogous closed conformation, the ribosomal structures with the full 241 complement of IRES/40S contacts (structure $6_{\Delta dII}$ - $9_{\Delta dII}$) show a striking difference between the 242 position of the head, from the closed conformation in structure $6_{\Delta dII}$ (matching the head position in 243 structures $1_{\Delta dII}$, $5_{\Delta dII}$) to the fully open state in structure $9_{\Delta dII}$ (Figure 2D-E). Although structures $7_{\Delta dII}$ 244 9_{Adll} have a canonically bound IRES with domain III contacting eS1, eS27 and ES7 as in structure 245 6_{AdII} , they show large-scale conformational changes to the head as the 40S subunit transitions from 246 semi-closed (structure $7_{\Delta dII}$) to fully open (structure $9_{\Delta dII}$) states. Thus, structure $7_{\Delta dII}$ opens by 3.9°, 247 structure $8_{\Delta dII}$ by 8.1° , and structure $9_{\Delta dII}$ by 10.0° compared to the conformation of the 18S rRNA 248 in structures $1_{\Delta dII}$ - $6_{\Delta dII}$. These global changes to the position of the 40S head are reflected in changes in the P site as the distance between U_{1248} and C_{1701} increases from 7.3 Å, to 9.9 Å and finally to 249

250 11 Å in structures $7_{\Delta dII}$, $8_{\Delta dII}$ and $9_{\Delta dII}$, respectively. Thus, this series of structures shows that even 251 in the absence of domain II, establishment of the full complement of IRES/40S contacts results in 252 the transition of the 40S subunit from the closed to the open state, which is required for 253 accommodation of the initiation codon and surrounding regions in the mRNA-binding channel. 254

254

255 Accommodation of the IRES in the mRNA-binding channel

256 In contrast to 40S/IRES binary complexes assembled on the AdII IRES, which showed 257 remarkable differences in the position of the 40S subunit head, binary complexes assembled on 258 the wt IRES yielded a uniform structure that was refined to 3.8 Å resolution from 119,320 particles 259 (structure 10_{wt}) (Figure 1B). Both the conformation of the 40S subunit and the structure of IRES 260 domains IIIa-f in structure 10_{wt} are identical to those in the open state of the $40S/IRES_{\Delta dII}$ binary complex (structure $9_{\Delta dII}$) (Figures 3A-B). There is, however, additional density that corresponds 261 262 to IRES domain II inserted into the 40S subunit E site, in a conformation that was observed in 263 purified IRES/80S complexes (Quade et al., 2015; Yamamoto et al., 2015). Superposition of 264 structure 10_{wt} and a closed-state 40S subunit shows that in the latter, steric clashes between uS7 265 and domain II would prevent insertion of this domain into the E site. Thus, domain II locks the 40S subunit into an open state, which is not similarly imposed in the case of the Δ dII IRES. 266

267 For the wt IRES, we also obtained the structure of the 40S•IRES•eIF1A ternary complex that was refined to 3.8 Å resolution from 204,320 particles (structure 11_{wt}, Figure 1B). The 268 269 conformation of the 40S subunit and the position of the IRES in it were identical to those in the 270 40S/IRES_{wt} binary complex (structure 10_{wt}) (Figures 3A-B). The complex clearly showed density 271 for eIF1A located between 18S rRNA helix (h) 44 and the ribosomal proteins eS30 and uS12, 272 allowing us to model the OB domain and the C-terminal subdomain of eIF1A (residues 22-122). 273 Although structure 11_{wt} lacks tRNA and the 40S subunit is in the open state, the position of eIF1A 274 on the ribosome as well as its overall conformation are identical to those in the structures of eIF2-275 containing 48S complexes (Brito Querido et al., 2020; Simonetti et al., 2020).

As expected, binary complexes assembled on the Δ dII IRES and containing the 40S subunit in the closed conformation (1 Δ dII-6 Δ dII) do not have mRNA in the mRNA-binding channel. However, although structures 9 Δ dII, 10_{wt} and 11_{wt} all have 40S subunits in the identical open conformation that is required for loading of mRNA into the channel, they differ strongly in the degree of ribosomal accommodation of the initiation codon and surrounding regions (Figure 3C). 281 In the 40S/IRES_{Δ dII} binary complex (structure 9_{Δ dII}), clear mRNA density was seen only in the exit 282 portion of the channel up to the -8 position of mRNA (HCV nt 334), after which the mRNA became 283 disordered (Figure 3D). In contrast, in the wt 40S/IRES binary complex (structure 10_{wt}), mRNA 284 nucleotides could be identified at the exit channel through the E site where it is stabilized by 285 domain II, to AU₃₄₂₋₃ located in the P site (Figure 3E). The (+3) nucleotide linked to U₃₄₃ could 286 not be identified due to disorder in the map. However, there is additional mRNA density in the 287 mRNA channel ~8 Å from the P-site G₃₄₄, but the identity of these nucleotides does not correspond 288 to those that immediately follow the start codon (A₃₄₅ onwards) as this density extends 20Å out 289 from the mRNA channel beyond the binding site of eIF1A, suggesting that after the P site, the 290 mRNA is looped out (Figure 3E). Thus, the presence of domain II results in insertion of mRNA 291 into the entire channel, but only the additional 9 nucleotides from the exit to the P site (i.e., from 292 G₃₃₅ to U₃₄₃) can be reliably identified. Density corresponding to mRNA is present from the P site 293 and entry channel but is likely a mixture of different registers of mRNA and so the sequence could 294 not be determined (Figure 3E). Strikingly, the presence of eIF1A in ribosomal complexes resulted 295 in accommodation of sequential mRNA along the entire mRNA binding cleft (Figure 3F). 296 Examination of critical P-site nucleotides for all complexes shows that in each case C₁₇₀₁ of 18S 297 rRNA is in a single conformation, except for the binary complex prepared with the wt IRES 298 (structure 10_{wt}) where it is present in two states as determined by examination of the Coulomb 299 potential around that nucleotide (Figure 3G). In the conformation of the second state, C_{1701} contacts 300 the upstream mRNA base U₃₄₃, possibly contributing to stabilizing the mRNA when it has not 301 undergone complete accommodation in the mRNA channel at the P site. The highly conserved 302 C₁₆₉₈ (Prince et al., 1982) contacts downstream mRNA and may act as a sensor to stimulate C₁₇₀₁ 303 adopting the second conformation in which it can stabilize the incompletely loaded mRNA (Figure 304 3G).

The position of the mRNA in structures 10_{wt} and 11_{wt} , however, does not match its position in 48S complexes with an established codon-anticodon interaction (Brito Querido et al., 2020; Simonetti et al., 2020). Beginning from the (-1) position, the following (+1), and (+2) nucleotides are ~4 Å above their position when tRNA is inserted (Figures 3H-I). However, the raised position of these nucleotides in the complex containing eIF1A nevertheless allows the (+4) adenine base to form the stacking triple with eIF1A Trp70 and 18S rRNA A₁₈₂₅ (Figure 3I), which is a key function

of eIF1A (Battiste et al., 2000). These contacts are maintained up to formation of 48S complexes
(Simonetti et al., 2020).

313 Taken together, the structures of binary complexes assembled on Δ dII and wt IRESs and 314 the eIF1A-containing complex assembled on the *wt* IRES provide structural rationalization for the 315 roles of domain II and eIF1A in sequentially loading the mRNA channel. Even without domain II, 316 binding of the IRES induces conformational changes in the 40S subunit that are required for 317 accommodation of mRNA in the binding channel. However, accommodation in this case is only 318 partial, and the 40S subunit is not stably present in the open conformation, which is consistent, on 319 one hand, with the ability of Δ dII IRES to function in initiation, but on the other hand, with lower 320 initiation activity than the wt IRES (e.g., Reynolds et al., 1996). The presence of domain II results 321 in accommodation of the initiation codon and the upstream region in the mRNA-binding channel, 322 thereby enhancing the efficiency of initiation (Reynolds et al., 1996), whereas addition of eIF1A 323 results in further accommodation of the mRNA in the entire mRNA-binding channel, accounting 324 for its enhancement of initiation on the IRES (Jaafar et al., 2016).

325

326 The structure of eIF2-containing 48S complexes assembled on the HCV IRES

327 The structures of eIF2-containing 48S ICs assembled on the wt and AdII IRES were refined from 46,904 and 103,813 particles to resolutions of 3.6 and 3.5 Å, respectively (structures 12_{wt} 328 329 and $12_{\Delta dII}$, Figures 1B and S1). Both wt and ΔdII IRES 48S ICs form identical complexes with respect to the 40S subunit's closed conformation, the positions of Met-tRNA_i^{Met}, eIF2 and eIF1A, 330 331 and the established P-site codon-anticodon base pairing (Figures 4A, and S5A-B). The IRES-332 containing 48S IC is also structurally identical to the canonical 48S complex formed by cap-333 dependent initiation (e.g., Simonetti et al., 2020) with respect to the global conformation of the 40S subunit as well as the placement of Met-tRNA_i^{Met}, eIF2α, and eIF1A. Thus, the E site-334 335 associated eIF2a contacts the highly conserved uS7/Asp194 directly and interacts with MettRNAi^{Met} via Thr103, Arg67 and His114 (Figure 4B). As with yeast 48S ICs (Hussain et al., 2014), 336 337 eIF2a forms hydrogen bonds with the (-3) adenosine via Arg55, a contact that enhances codon 338 selection in the scanning mode of initiation, presumably by stabilizing the arrested 48S IC (Pisarev et al., 2006; Thakur et al., 2020). Contacts between eIF2α Arg57 and the tRNA acceptor stem loop 339 340 (ASL) and the 18S rRNA that occur in canonical 48S ICs are also present (Simonetti et al., 2020) 341 (Figure 4B). The position of eIF2 α is identical in *wt* and Δ dII IRES 48S ICs (Figure S5E). The

unsharpened map also contained density corresponding to $eIF2\gamma$ (Figure S5D) identical to that seen in cap-dependent 48S initiation complexes (Simonetti et al., 2020), but it had a low local resolution at the acceptor end of Met-tRNA_i^{Met} and was not modelled after map sharpening.

345 The position of domain II differs substantially between the 48S IC assembled on the wt 346 IRES (structure 12_{wt}) and the corresponding 40S/IRES binary and 40S/eIF1A/IRES ternary 347 complexes (structures 10_{wt} and 11_{wt}). In both the binary and ternary complexes, it is inserted into 348 the E site, a position that is incompatible with the binding of eIF2. Thus, in the 48S IC, domain II 349 is oriented away from the subunit interface, towards the solvent side of the 40S subunit, and shows 350 an attenuation of density so that a model of domain II is not fully enclosed by the map. Focused 351 classification of this region revealed that domain II is flexible and occupies multiple conformations 352 oriented away from the E site (Figure 4C; Figure S5F; Table S5).

Compared with the binary or ternary complexes (structures 10_{wt} and 11_{wt}), the head of 48S ICs formed on both *wt* and Δ dII IRESs is in a closed position, having moved by 11.2° relative to the open states (Figure 4D), and is in an even more closed conformation than in closed binary complexes (structures $1_{\Delta dII}$ - $6_{\Delta dII}$), in which the position of the head differed from that in structures 10_{wt} and 11_{wt} by ~9.0° (Figure 3A).

358 Comparison between the ternary complex (structure 11_{wt}) and the 48S IC (structure 359 $12_{wt/AdI}$) shows the effect that incorporation of tRNA into the P site and rearrangement of 18S 360 rRNA into the closed conformation has on the position of mRNA in the mRNA-binding channel. 361 The raised position of P-site mRNA in the ternary complex (Figure 4E) cannot be maintained as 362 this would cause a clash with the P-site tRNA in the 48S IC (Figure 4F). Thus, upon 40S subunit closure and incorporation of P-site tRNA, the mRNA repositions ~4 Å deeper into the mRNA 363 364 channel and the A(+4) base flips out to maintain the stacking triple with eIF1A Trp70 and 18S 365 rRNA A₁₈₂₅ that is seen in the ternary complex (Figures 4E-F). The mRNA is also shifted upstream 366 due to the movement of eS28 in the ribosome head (Figure 4G). A network of hydrogen bonds in 367 the ternary complex (structure 11_{wt}) between multiple arginines in eS28 and the mRNA is reformed 368 by the displacement of eS28 in the closed complex (structure $12_{wt/\Delta dII}$). Arg69 contacts the guanine 369 at (-7) position in the ternary complex, but the shift of the 18S rRNA to the closed position causes 370 this leading contact to be broken and reformed with G(-5). Other contacts are similarly 371 reorganized, and the Arg31 contact with the stacked G₃₃₁-G₃₀₇ pair is lost completely (Figure 4G-372 H). This reorganization of contacts causes the mRNA to shift by one base pair at the P site and

373 allows contact with the tRNA anticodon arm once tRNA is inserted into the P site. Interestingly, 374 eIF2 α Arg55 contacting the mRNA at A(-3) is in the same position as C₈₃ in IRES domain II in 375 the 40S/eIF1A/IRES ternary complex, which could indicate that this location in the E site is 376 important for stabilizing the mRNA regardless of the conformation of the 40S subunit and 377 differences in position of mRNA at other locations along the mRNA-binding channel (Figure 4I). 378 Interestingly, we also obtained 40S ribosomal complexes containing platform-bound wt or 379 Δ dII IRES and P-site Met-tRNA^{Met} but lacking all initiation factors (structures 13_{wt} and 13_{Δ dII}) 380 (Figure 1C). These closed complexes, refined from 15,906 and 15,598 particles to 4.6 and 4.4 Å, 381 respectively, clearly showed density for codon-anticodon base pairing (Figure S3G; Table S3). It 382 is unclear whether initiation factors dissociated due to slow eIF5-independent hydrolysis of eIF2-383 bound GTP (Unbehaun et al., 2004), or through denaturation at the air-water interface and/or due 384 to the shear forces associated with blotting (Glaeser, 2021; d'Imprima et al., 2019). In any case, 385 this complex likely mimics an intermediate state immediately after eIF2 dissociation and prior to 386 the binding of eIF5B.

- 387
- 388

The structure of eIF5B-containing 48S complexes assembled on the IRES

389 Classification of eIF5B-containing ribosomal complexes yielded two structures formed on 390 the wt IRES (structures 14_{wt} and 15_{wt}) and one structure (15_{Δ dII}) assembled on the Δ dII IRES 391 (Figures 1B and S1). Structures 14_{wt}, 15_{wt} and 15_{ΔdII} were refined to 3.8 Å, 3.7 Å and 3.7 Å 392 resolution from 60,578, 133,782 and 61,648 particles, respectively (Figures 5A-B and S6A). All structures contain eIF5B, eIF1A and the P-site Met-tRNA^{Met}. However, whereas structures 15_{wt} 393 394 and $15_{\Delta dII}$ showed density for the base-paired codon-anticodon and were accordingly classified as 48S ICs, the P-site Met-tRNA^{Met} was not base-paired with the initiation codon in structure 14_{wt}, 395 396 which was therefore designated as a pre-48S IC (Figure S3G). Similar to eIF2-containing 48S ICs 397 assembled on the wt IRES, in eIF5B-containing ICs assembled on the wt IRES (structure 15_{wt}) 398 domain II is oriented away from the subunit interface, toward the solvent side of the 40S subunit, 399 and shows an attenuation of density that can be resolved by focused classification into multiple 400 states (Figure 1B and S6B; Table S5). In contrast to structures 15_{wt/\DeltadII} that are in an identical 401 closed conformation, the 40S subunit in structure 14w is in an open conformation with domain II 402 inserted into the E site (Figure S6C). In all structures, eIF1A occupies its usual position over h44

and eS30 and uS12, whereas eIF5B resides on the intersubunit face of the 40S subunit as in 80S
ribosomal complexes (Yamamoto et al., 2014; Huang and Fernandez, 2020; Wang et al., 2020).

405 The structures show clear density for eIF5B residues 592-1218, corresponding to all major 406 domains. The G domain, and domains II and III form the central domains of eIF5B that connect 407 via domain III and helix 12 to the tRNA acceptor stem binding domain IV. (Figure 5C). This is 408 the first high-resolution structure of mammalian eIF5B and also the first structure of the 40S/eIF5B 409 subunit complex prior to subunit joining. Although we used full-length native eIF5B, extensive 410 3D classification and processing did not reveal any structure corresponding to the N-terminal 411 region, suggesting that the structure in this region is highly disordered, an observation that is supported by the structure of full-length eIF5B from a range of species predicted using AlphaFold 412 413 (Jumper et al., 2021). Consistent with the requirement of the 60S subunit for induction of eIF5B's 414 GTPase activity (Pestova et al., 2000), all complexes contained eIF5B-bound GTP (Figure S6E). Previous structures of mammalian eIF5B determined at ~9 Å resolution used GMPPNP and 415 416 showed the GDP-bound conformation of switch 1 (Yamamoto et al., 2014) (Figure S7A). In 417 contrast, all our complexes showed switch 1, switch 2, and the β - β 10 loop in domain II in the 418 GTP-bound conformation (Kuhle and Ficner, 2014). The conformation of this conserved GTP-419 binding region of mammalian eIF5B is identical to that in fungal eIF5B (Kuhle and Ficner, 2014; 420 Wang et al., 2020) (Figure S7B-D).

421 We identified multiple contacts between eIF5B domains II and III and 18S rRNA h5, h14, 422 and h15, as well as an interaction between eIF5B domain II and uS12 (Table S6; Figure S6D), and 423 noted that the β 13- β 14 loop in our complexes could interfere with the transition of switch 1 from 424 GTP-bound to GDP-bound conformations (Kuhle and Ficner, 2014) (Figure S6F). On the yeast 425 80S ribosome, the β 13- β 14 loop of eIF5B contacts A₄₁₅ in 18S rRNA h14 and is positioned away 426 from the path that switch 1 might take as it changes to the GDP-bound conformation (Wang et al., 427 2020). Although there is no contact between the equivalent nucleotide (A₄₆₄) and β 13- β 14 in our 428 complexes, h14 is accessible. These observations suggest that the 60S subunit might stimulate the 429 interaction between A_{415} and the $\beta 13$ - $\beta 14$ loop to reposition this loop away from switch 1 so that 430 a transition from GTP- to GDP-bound conformation. In both pre-48S ICs and 48S ICs, the position 431 of domain IV also allows it to contact eIF1A via interactions between His112 in the helical 432 subdomain of eIF1A (Battiste et al., 2000) and the extreme C-terminal region of eIF5B, as well as 433 between the eIF1A L23 beta-turn (near Gly54) and Arg1186 in domain IV of eIF5B (Figure 5D).

These interactions are distinct from the previously reported binding of eIF1A's extreme C-terminal
DDIDI sequence to the h12/h13 loop in eIF5B domain IV (Marintchev et al., 2003; Zheng et al.,
2014) and of the eIF1A L45 loop to eIF5B domain III (Nag et al., 2016).

Comparison of the position of the P-site Met-tRNA_i^{Met} in the eIF2-containing 48S IC 437 (Simonetti et al., 2020) and in the 80S ribosome (Yamamoto et al., 2014; Wang et al., 2020) shows 438 439 when the large subunit is present, tRNA rotates 14° towards the 40S subunit body and the T-loop 440 moves by ~ 15 Å to allow placement of the acceptor stem into the P site of the 60S subunit. We therefore examined our maps (structures $12_{wt/\Delta dII}$ - $15_{wt/\Delta dII}$) to determine how the orientation of the 441 P-site tRNA differs in 40S ribosomal complexes depending on the presence of eIF2 or eIF5B. 442 Compared to eIF2-containing 48S ICs, in eIF5B-containing complexes, Met-tRNAi^{Met} rotates by 443 444 \sim 14° and moves by 15 Å from the head of the 40S subunit to a position that matches the orientation seen in 80S structures (Wang et al., 2020) (Figure 5C). This repositioning of tRNA was observed 445 446 for all structures that contained eIF5B, regardless of whether the 40S subunit was in the open (pre-447 48S IC) or closed (48S IC) conformation (Figure 5C), indicating that eIF5B re-orients MettRNA;^{Met} on the 40S subunit at the 48S PIC stage prior to subunit joining. Interestingly, although 448 the overall position of eIF5B-Met-tRNA_i^{Met} in eIF5B-containing 48S ICs and in 80S ribosomes is 449 similar, upon binding of a 60S subunit, domain IV of eIF5B undergoes a 33° rotation towards the 450 451 platform side of the 40S subunit as well as a translation by 6.4 Å parallel to the mRNA channel 452 towards the platform of the 40S subunit, which results in repositioning of the tRNA acceptor stem 453 by 6.4 Å toward the ribosome head (i.e., toward ribosomal protein eS25) without changing the 454 position of the ASL (Figure 5E-F). The repositioning of eIF5B domain IV occurs despite an only 455 minor movement of helix 12 (Figure 5F; Figure S6G). Such repositioning of domain IV and the 456 tRNA acceptor stem upon binding of a 60S subunit would avert steric clashes of domain IV with 457 H84 of 28S rRNA and between uL16 and the tRNA acceptor stem (~A74) (Figure 5F). Similar 458 repositioning of IF2 domain C2 (equivalent to eIF5B domain IV) to avoid analogous steric clashes 459 was observed in bacteria upon joining of 50S subunits to 30S ICs (Hussain et al., 2016). 460 Adjustment of the orientation of initiator tRNA prior to subunit joining is a critical step in 461 initiation, and the mechanism by which it is mediated, by rotation and translation of domain IV of 462 the universally conserved initiation factor IF2/eIF5B, likely appeared early in evolution.

463 Despite the differences in the orientation of the acceptor arm of the P-site tRNA in 464 ribosomal complexes containing eIF2 and eIF5B, as well as differences in the conformation of the

465 40S subunit in eIF2/eIF5B-containing 48S ICs and eIF5B-containing pre-48S ICs, the anticodon 466 loop in all these complexes is identically positioned (Figure 5D). eIF5B- and eIF2-containing 48S 467 ICs assembled on the IRES are also in the same closed conformation (Figures S6C), identical to 468 that in 48S ICs assembled on canonical cap-dependent mRNA (Simonetti et al., 2020). Thus, in 469 eIF5B- and eIF2-containing 48S ICs, 18S rRNA nucleotides C1701 and U1248 are separated by ~3.5 470 Å, and the contacts of the P-gate nucleotides G₁₆₃₉ and A₁₆₄₀ in the 18S rRNA and Arg146 in uS9 471 with the tRNA anticodon arm on the opposite side to the anticodon are also present in both 48S 472 ICs.

473 In contrast, the 40S subunit in the eIF5B-containing pre-48S IC is in the open 474 conformation, in which the separation between C_{1701} and U_{1248} is increased to ~11 Å, and there are 475 no contacts between the tRNA and the P gate or uS9 (Figure 5H). As with the 40S/eIF1A/IRES 476 ternary complex (structure 11_{wt}), the open configuration of the ribosome head present in the pre-477 48S IC creates a network of hydrogen bonds between the mRNA and eS28 (Figure S7E) that causes 478 the mRNA to be shifted by one nucleotide relative to the closed configuration (Figure S3G). This 479 results in the final nucleotide of the start codon (G_{344}) being out of place in the P site and not 480 participating in any contacts with the tRNA anticodon. Instead, G₃₄₄ is available to form a stacking 481 triple with eIF1A Trp70 and A₁₈₂₅ of 18S rRNA (Figure 5H). In the closed conformation of 48S 482 ICs, the hydrogen bonds with eS28 have been partially broken (Figure S7F) and so all three 483 nucleotides of the start codon are accommodated in the P site, and the A(+4) nucleotide is available 484 to form a stacking triple with eIF1A Trp70 and A1825 of 18S rRNA (Figure 5F and 5I).

485

486 Comparison of eIF5B-containing pre-48S initiation complexes with eIF2-containing scanning 487 43S complexes

488 In contrast to initiation on the HCV IRES, eIF5B cannot substitute for eIF2 in recruiting Met-tRNAi^{Met} to the 40S subunit in the canonical scanning mechanism. Canonical initiation also 489 490 requires eIF1, which binds to the 40S subunit below the mRNA channel at the P site between h24 491 and the region connecting h44 to h45 and, in cooperation with eIF1A, induces the open 492 conformation of the 40S subunit (Passmore et al., 2007; Llácer et al., 2015), thereby promoting 493 ribosomal attachment to mRNA, scanning and initiation codon selection (e.g., Pestova and 494 Kolupaeva, 2002). We therefore compared the conformation of the 40S subunit and the positions of mRNA and Met-tRNA;^{Met} in eIF5B-containing pre-48S complexes formed on the wt IRES 495

496 (structure 14_{wt}) and in canonical scanning eIF2-containing 43S complexes that also contained eIF1
497 (Brito Querido et al., 2020).

498 Even though the individual mRNA bases could not be identified in the scanning, eIF2-499 containing 43S complex because the P site nucleotides were heterogenous (Brito Querido et al., 500 2020), the positions of mRNA in this complex and in the eIF5B-containing pre-48S complex are very similar (Figure 6A). Although codon-anticodon base-pairing is not established in either 501 502 complex, the anticodon loops of Met-tRNA^{Met} in both are poised to contact mRNA and base-pair with an initiation codon, which is in contrast to the POUT position of tRNA in fully open mRNA-503 504 free 43S complexes (Kratzat et al., 2021), in which the anticodon loop is positioned too far away 505 to be able to interact with mRNA if it had bound in the P site (Figure S7G). However, whereas the 506 conformations of the anticodon in the P site in both complexes are similar, in the eIF5B-containing 507 complex, the T-arm and the acceptor stem are shifted toward the body of the 40S subunit by 508 bending of the anticodon loop region (Figure 6B). Consequently, the contacts between the ASL of 509 Met-tRNAⁱ^{Met} and 18S rRNA nucleotides GA₁₆₃₉₋₄₀ and the N-terminal region of uS9 in the head 510 of the 40S subunit, which are present in all eIF2-containing complexes, including mRNA-free and 511 scanning 43S complexes and 48S ICs (e.g., Hussain et al., 2014; Brito Querido et al., 2020; 512 Simonetti et al., 2020), do not exist in the eIF5B-containing pre-48S ICs and only form after codon-513 anticodon base-pairing (Figure 6B). Thus, interaction with eIF2 allows tRNA to maintain the 514 contacts with the head of the 40S subunit in all conformations, from fully open to fully closed, and 515 the position of the anticodon loop that allows it to inspect mRNA in the scanning 43S complexes 516 is determined by the rotation of the head that is in the intermediate conformation compared to fully 517 open and fully closed states. In contrast, when interacting with eIF5B, tRNA establishes these 518 contacts only in the closed position of the head, whereas in the open pre-48S ICs tRNA is stabilized by contacts between eIF5B domain IV and the acceptor stem, tRNA anticodon U₃₅ and mRNA 519 520 A(+1), and a single 18S rRNA nucleotide (C_{1701}) that partially stacks with C_{33} (instead of the 521 stacking of both U_{1248}/C_{1701} as in the closed case) (Figure 6B). Thus, whereas some aspects of 522 eIF5B-containing pre-48S complexes are analogous to those of eIF2-containing scanning 43S 523 complexes, the overall orientation, and the specific interactions of tRNA in them differ.

In eIF5B pre-48S complexes, the open conformation of the 40S subunit is supported by the insertion of IRES domain II into the E site, whereas in eIF2-containing complexes, the conformation of the 40S subunit is determined by the binding of eIF1. We therefore analyzed

527 whether binding of eIF1 would be compatible with the structure of eIF5B-containing pre-48S ICs. The position of eIF1 placed into such complexes suggests that it would clash with tRNA. Thus, 528 529 the repositioning of tRNA in eIF5B-containing complexes causes the AAC₃₈₋₄₀ nucleotides of MettRNA_i^{Met} to move toward the 40S subunit body by \sim 3.0 Å, so that the binding of eIF1 as in the 530 531 43S scanning complex would create a clash between A_{36} of Met-tRNA_i^{Met} and the β 1- β 2 loop 532 (Figure 6C). Accommodation of eIF1 would require either reorganization of this loop or 533 displacement of the P-site tRNA. Examination of human (Fletcher et al., 1999) and yeast (Reibarkh 534 et al., 2008) solution NMR structures of eIF1 did not identify any conformations of the β1-β2 loop 535 that would allow a clash with the anticodon stem of tRNA to be avoided in the eIF5B-containing 536 pre-48S and 48S ICs. Moreover, the eIF1 β 3- β 4 loop would also clash with tRNA nucleotides 537 GU₂₃₋₂₄, and a clash between Phe113 and tRNA nucleotide G₂₅ is also possible (Figure 6C). These observations suggest that even if eIF5B were able to bind Met-tRNAi^{Met} with high affinity and 538 539 recruit it to the 40S subunit efficiently, the structure of the resulting complexes would not be 540 compatible with binding of eIF1 and hence, with the scanning mechanism of initiation. On the other hand, the stabilizing interaction of the acceptor arm of Met-tRNAi^{Met} with domain IV of 541 542 eIF5B in the closed 48S complexes following dissociation of eIF2•GDP and eIF1 would lock the 543 complex preventing leaky scanning from occurring.

544 The incompatibility of Met-tRNAi^{Met} and eIF1 on eIF5B-containing pre-48S complexes 545 likely explains why eIF1 disrupts 48S complexes prepared using wt but not the Δ dII variant of the 546 HCV-like CSFV IRES (Pestova et al., 2008). HCV domain II has the propensity to insert into the 547 E site (Quade et al., 2015; Yamamoto et al., 2015), locking the ribosome into the open 548 conformation, and the structurally related CSFV domain II likely behaves similarly. As outlined 549 above, the tRNA consequently loses contacts with uS9, with $GA_{1639-40}$ as well as with U_{1248} . If 550 eIF1 binds to this complex, then the insertion of its $\beta_{1-\beta_{2}}$ loop into the mRNA channel creates 551 steric hindrance between mRNA and tRNA in the P site, dislodging the tRNA.

552 CONCLUDING REMARKS

Here we present the most comprehensive structural overview of the HCV IRES-mediated initiation pathway to date (Figure 7). The IRES initially binds to the 40S subunit through domains IIIa/IIIc and then pivots onto its platform side where it establishes the complete set of contacts (structures $1_{\Delta dII}-6_{\Delta dII}$). Once the canonical set of contacts are made, this induces the head of the ribosome to open (structure $8_{\Delta dII}-9_{\Delta dII}$). Although head opening can occur in the absence of IRES

558 domain II, such complexes are nevertheless characterized by remarkable heterogeneity in the 559 position of the 40S subunit head. In contrast, 40S/IRES binary complexes assembled on the wt 560 IRES yield a uniform structure, in which the 40S subunit is in the open conformation, and domain II is inserted into the E site (structure 10_{wt}). Importantly, in the absence of domain II, mRNA 561 562 density was clearly seen only in the exit portion of the channel up to the -8 position of mRNA 563 (structure $9_{\Delta dII}$), whereas in the wt 40S/IRES binary complex, mRNA nucleotides could be 564 identified at the exit channel through the E site where it is stabilized by domain II, to AU₃₄₂₋₃ 565 located in the P site (structure 10_{wt}), and eIF1A induces further accommodation of the mRNA in 566 the entire mRNA-binding channel (structure 11_{wt}). Thus, these complexes provide structural 567 insights into the functions of multiple IRES domains, including IIIa/IIIc in establishing the initial 568 ribosome contacts, IIId in fixing the IRES to the 40S subunit and inducing ribosomal head opening, 569 and II in imposing the open conformation and promoting fixation of mRNA in and upstream of 570 the P site. Our analysis also revealed the role of eIF1A in completing mRNA accommodation.

Once the mRNA is loaded, initiation can proceed either along the canonical initiation 571 pathway, in which eIF2 promotes attachment of Met-tRNAi^{Met} to form the 48S IC (structure 572 573 12_{wt/\ddII}) and then dissociates after GTP hydrolysis (likely structure 13_{wt/\ddII}) followed by binding of eIF5B (structure 15_{wt/\dll}), or by a shortcut route, in which Met-tRNA_i^{Met} is loaded directly by 574 575 eIF5B, first forming open pre-48S ICs without established codon-anticodon interaction (structure 576 14_{wt}) and then locking upon codon-anticodon base-pairing (structure 15_{wt}). The eIF2-containing 577 48S ICs assembled on the IRES are structurally identical to canonical 48S ICs with respect to the conformation of the 40S subunit and the positions of Met-tRNA_i^{Met}, eIF2 and eIF1A. The position 578 579 of domain II of the IRES in 40S/IRES_{wt} binary complexes is incompatible with binding of eIF2 580 and the closed conformation of the 40S subunit, and consequently, in 48S ICs, domain II is oriented 581 away from the subunit interface, toward the solvent side, occupying multiple conformations 582 oriented away from the E site. In eIF5B-containing pre-48S ICs, the 40S subunit is in the open 583 conformation and domains II is inserted into the E site. Upon codon-anticodon base-pairing in 584 eIF5B-containing 48S ICs, the 40S subunit adopts the closed conformation, and domain II 585 becomes displaced from the E site and is oriented away from the subunit interface like in eIF2-586 containing 48S ICs. Importantly, compared to eIF2-containing 48S ICs, in eIF5B-containing pre-48S ICs and 48S ICs, Met-tRNA_i^{Met} rotates by $\sim 14^{\circ}$ and moves 15 Å from the head of the 40S 587 588 subunit to a position that matches the orientation in 80S ribosomes. Thus, our data show how

621 Acknowledgments

- 622 This work was supported by NIH R01 GM55440 (to J.F.), R35 GM139453 (to J.F.), R35
- 623 GM122602 (to T.V.P.), and R01 AI123406 (to C.U.T.H.) Cryo-EM data were collected at the
- 624 Columbia University Cryo-Electron Microscopy Center.

625 Author Contributions

- 626 Conceptualization, T.V.P., C.U.T.H., and J.F.; Investigation, Z.P.B., and I.A.; Validation Z.P.B.,
- 627 I.A., and S.D.; Writing Original Draft, T.V.P. and Z.P.B.; Writing Review and Editing, Z.P.B.,
- 628 I.A., S.D., C.U.T.H., T.V.P., and J.F.; Funding Acquisition, C.U.T.H., T.V.P., and J.F.;
- 629 Supervision, C.U.T.H., T.V.P., and J.F.

630 Declaration of Interests

- 631 Authors declare no competing interests.
- 632
- 633
- 634
- 635
- 636
- 637
- 638
- 639
- 640
- 641
- 642
- 643
- 644
- 645
- 646
- 647
- 648
- 649
- 650

651

652 FIGURE LEGENDS

653

654 Figure 1. Overview of HCV IRES-mediated initiation complexes.

- 655 (A) Secondary structure of the HCV IRES.
- (B) Segmented maps of labeled IRES ICs, showing the 40S subunit (yellow), IRES (red), eIF1A
- 657 (blue), Met-tRNA_i^{Met} (magenta), and initiation factors eIF2 or eIF5B (green). Complexes were
- assembled on the *wt* or Δ dII IRES. Complexes that share identical 40S subunit conformation and
- 659 factor composition are enclosed by dashed lines.
- 660 (C) Contacts between the IRES and 40S subunit. Ribosomal proteins (red), 18S rRNA (yellow),
- and the AUG codon (blue) are marked for the labeled complexes. Complete pathway in Figure S4and Table S4.
- 663 See also Figures S1-S4 and Tables S1-S4.
- 664

Figure 2. Initial events during binding of the HCV IRES to the 40S subunit.

666 (A) IRES models from structures $1_{\Delta dII}$ - $6_{\Delta dII}$ aligned on the 40S subunit. IRES domains and

ribosomal proteins eS1 (blue), eS27 (magenta) and 18S rRNA ES7 (yellow) are indicated (inset).

- 668 **(B)** Comparison between minimally bound (structure $1_{\Delta dII}$) and fully bound (structure $6_{\Delta dII}$) IRES 669 complexes showing the displacement of labeled IRES domains.
- 670 (C) Formation of critical contacts between ES7 and the IRES requires reorganization of domains
- 671 hIII₁, IIIe, and IIId. The arrows indicate displacement of IRES nucleotides A₁₃₆ (hIII₁), G₂₉₅/A₂₉₆
- 672 (IIIe) and GGG₂₆₆₋₂₆₈ (IIId) interacting with ES7 from the minimally bound (structure $1_{\Delta dII}$) to the
- 673 fully bound state (structure $6_{\Delta dII}$) indicated with a prime (').
- 674 **(D)** RMSD (Å) of 18S rRNA for complexes labeled as in (E) compared to the minimally bound 675 state (structure $1_{\Delta dII}$), color-coded as in the inset key. The angle formed between helix 33 (h33')
- and helix 28 (h28') in structure $1_{\Delta dII}$ and helix 33 (h33'') in the labeled complex is also marked.
- 677 (E) Segmented maps for labeled complexes showing 40S subunit (yellow) and IRES (red)
- 678 organized in a putative sequence showing the minimally bound state (structure $1_{\Delta dII}$), canonical
- 679 IRES binding (structure $6_{\Delta dII}$) and the induction of opening of the head of the 40S subunit (structure
- $680 \quad 7_{\Delta dII} 9_{\Delta dII}).$
- 681 See also Figure S4 and Table S4.
- 682

683 Figure 3. IRES domain II is required for loading mRNA into the mRNA channel

- (A) RMSD (Å) of 18S rRNA for complexes labeled as in (B) compared to the minimally bound
- state (structure $1_{\Delta dII}$), color-coded as in the inset key. The angle formed between helix 33 (h33')
- and helix 28 (h28') in structure $1_{\Delta dII}$ and helix 33 (h33'') in the labeled complex is also marked.
- 687 (B) Segmented maps for labeled complexes showing 40S subunit (yellow), IRES (red), and eIF1A
- (blue) organized in a putative sequence showing the minimally bound state (structure $1_{\Delta dII}$), fully
- opened head of the 40S subunit (structure $9_{\Delta dII}$), binary complex (structure 10_{wt}), and the eIF1A-
- 690 containing ternary complex (structure 11_{wt}).
- 691 (C) Diagram of structures $1_{\Delta dII}$, $9_{\Delta dII}$, 10_{wt} and 11_{wt} showing the sequential loading of mRNA into 692 the mRNA channel.
- 693 (**D-F**) The mRNA channel spanning the entry and exit channels, A, P, and E sites viewed through
- the ribosome head towards the body for the labeled complexes. The IRES (red), Coulomb potential
- 695 (blue mesh), and eIF1A (blue) are shown.
- 696 (G) Position of key nucleotides in the P site in structure 10_{wt} showing interactions between
- 697 incompletely loaded mRNA and C_{1698} resulting in C_{1701} sampling dual conformations near the (+2) 698 position.
- 699 (H-I) P site showing mRNA interactions for the (H) binary complex (structure 10_{wt}) and the (I)
- 700 eIF1A-containing ternary complex (structure 11_{wt}). 18S rRNA (yellow), eIF1A (blue), IRES
- 701 mRNA (red) with start codon (cyan) are all marked. The position of mRNA modelled in the 48S
- 702 cap-dependent IC (PDB: 6ZMW) is shown in grey.
- 703

704 **Figure 4. The HCV IRES•eIF2-containing 48S initiation complex.**

- 705 (A) Overview of the *wt* IRES eIF2-containing 48S IC (structure 12_{wt}).
- 706 **(B)** Contacts between eIF2 α and HCV IRES, Met-tRNA_i^{Met}, and 40S subunit.
- 707 (C) IRES domain II occupies multiple positions in the eIF2-containing 48S IC.
- (D) Position of 18S rRNA in the open ternary complex (structure 11_{wt}) and eIF2-containing 48S
 IC (structure 12_{wt}).
- 710 (E-F) The P site in the (E) ternary complex (structure 11_{wt}) and the (F) eIF2-containing 48S IC
- 711 (structure 12_{wt}) showing 18S rRNA (yellow), Met-tRNA_i^{Met} (magenta), eIF1A (blue), and IRES
- 712 mRNA (red) with the start codon (cyan) marked. (E) The position of mRNA in the cap-dependent
- 713 48S IC is marked (grey).

- 714 (G-H) Contacts between eS28 (salmon) and the IRES (red) in (G) the ternary complex (structure
- 715 11_{wt}) and (H) the eIF2-containing 48S IC (structure 12_{wt}).
- (I) Global conformation of mRNA in the ternary complex (structure 11_{wt}) and the eIF2-containing
- 48S IC (structure 12_{wt}). The arrow indicates the extent of movement of eS28 between the binary
- 718 complex (structures 11_{wt}) and the eIF2-containing 48S IC complex (structure 12_{wt}).
- 719 See also Figure S5 and Table S5.
- 720

721 Figure 5. The HCV IRES•eIF5B-containing 48S initiation complex

- 722 (A) Overview of the *wt* IRES eIF5B-containing pre-48S IC (structure 14_{wt}).
- 723 **(B)** Overview of the *wt* IRES eIF5B-containing 48S IC (structure 15_{wt}).
- 724 (C) Changes to the position of P site tRNA depending on the presence of either eIF2 or eIF5B.
- 725 Upon binding of eIF5B, the T-arm, D-arm and acceptor stem of Met-tRNA_i^{Met} move by 15.6 Å
- and 14° relative to their positions in the eIF2-containing 48S complex.
- 727 (D) Inset showing the conformation of tRNA acceptor stem loop, and contacts between eIF5B
- domain IV and eIF1A. The conformation of the ASL is unchanged between the pre-48S IC(eIF5B), and the 48S IC (eIF2 or eIF5B).
- (E) Position of eIF5B and tRNA in the 48S and pre-elongation 80S ribosome complexes. eIF5B
 undergoes relatively little movement between the 48S (green) and 80S stages (red) in the II, G,
 and III domains, but domain IV translates and rotates (see F) causing movement in the tRNA
 between the two complexes (magenta and orange respectively). Arrows show displacement for
 labeled domains or components between the eIF5B-containing 48S IC and pre-elongation 80S
- ribosome.
- 736 (F) The position of eIF5B domain IV in the 48S IC (green) would clash with 28S rRNA H89 and
- vL16 in the 60S subunit. Upon binding of the 60S subunit, eIF5B domain IV (red) translates by
- 738 6.4Å towards to the platform side of the 40S subunit and rotates by 30.9° causing the tRNA to
- rotate by 12.4° and translate by 6.4° towards the head.
- 740 (G-I) P site for (G) eIF2-containing 48S IC (structure 12_{wt}), (H) eIF5B-containing pre-48S IC
- 741 (structure 14_{wt}), and (I) eIF5B-containing 48S IC (structure 15_{wt}) showing 18S rRNA (yellow),
- 742 Met-tRNA_i^{Met} (magenta), eIF1A (blue), and IRES mRNA (red) with the start codon (cyan) marked.
- 743 See also Figures S6-S7 and Tables S5-S6.
- 744

745 Figure 6. Position of mRNA in the ribosomal P-site and codon-anticodon recognition.

- 746 (A) Position of tRNA in the P site for the P_{OUT} complex (PDB: 7A09) (blue), 43S scanning
- complex (PDB: 6ZMW) (yellow), and the pre-48S IC (structure 14_{wt}) (magenta). mRNA from the
- 43S scanning complex (green) and pre-48S IC (red) is shown.
- 749 (B) Contacts between tRNA, the initiation codon and the P site for the labeled complexes.
- 750 (C) The β 1- β 2 and β 3- β 4 loops of eIF1 bound as in the 43S scanning complex (PDB: 6ZMW)
- 751 would clash with the pre-48S IC position of Met-tRNA_i^{Met}.
- 752 See also Figure S7.

754 Figure 7. The HCV IRES-mediated initiation pathway.

Ribosomal complexes organized in a putative IRES-mediated initiation pathway. Maps are
segmented showing the 40S subunit (yellow), IRES (red), eIF1A (blue), Met-tRNA_i^{Met} (magenta),
and eIF2 or eIF5B (green).

776 SUPPLEMENTARY FIGURE LEGENDS

777

778 Figure S1. Classification of HCV IRES containing ribosomal complexes, related to Figure 1.

- (A-D) Example micrographs for (A) the wt eIF2-containing sample, (B) the wt IRES eIF5B-
- containing sample, (C) the Δ dII IRES eIF2-containing sample, and (D) the Δ dII IRES eIF5B-
- 781 containing sample. Further details in Table S2. Scale bar 2000 Å.
- (E) Example 2D classification results for the *wt* IRES eIF2-containing sample.
- 783 (F-G) Classification scheme for (F) wt IRES and (G) Δ dII IRES containing samples. For full details
- regarding classification see methods. Final maps are colored showing the 40S subunit (yellow),
- 785 IRES (red), eIF1A (blue), Met-tRNA^{iMet} (magenta), and initiation factors eIF2 or eIF5B (green).
- Full details for complexes are available in Table S3 (structures $1_{\Delta dII}$ -15_{wt/ ΔdII}), Table S5 (16_{wt}-28_{wt}),
- and Table S7 (structures 29_{wt} - $46_{\Delta dII}$).
- 788

789 Figure S2. Local resolution, related to Figure 1.

- 790 (A) Local resolution of labeled HCV IRES complexes.
- 791 (B) Central slice of each complex.
- 792 Local resolution values and filtered maps can be found under EMDB ascension codes for each
- 793 structure (see Table S3).
- 794

795 Figure S3. Example densities, related to Figure 1.

- (A) Domain IIId (red) and ES7 (yellow) for the pre-48S IC (structure 14_{wt}).
- (B) Domain IIId (red) and ES7 (yellow) for the minimally bound complex (structure $1_{\Delta dII}$)
- 798 (C) Contact between domain IIIa/IIIc (red) and riboprotein eS27 (magenta) in the ternary complex
- 799 (structure 12_{wt}).
- 800 (**D**) eIF2 alpha helix 1 in the *wt* IRES 48S IC (structure 12_{wt}), top, and the ΔdII IRES 48S IC
- 801 (structure $12_{\Delta dII}$), bottom.
- 802 (E) eIF5B alpha helix 12 in the eIF5B-containing pre-48S IC (structure 14_{wt}), top, and the 48S IC
- 803 (structure 15_{wt}), bottom.
- 804 (F) eIF1A example densities from the eIF5B-containing pre-48S IC (structure 14_{wt}), left, and the
- 805 eIF2-containing 48S IC (structure 12_{wt}), right.

806 (G) Initiation codon (red) and tRNA anticodon (magenta) for all complexes where mRNA is 807 present in the P site. Diagram shows identity of nucleotides and hydrogen bonds for tRNA and

- 808 initiation codon bases in each accompanying figure.
- 809

810 Figure S4. Interactions between HCV IRES and 40S ribosomal subunit for all complexes,

811 related to Figures 1 and 2.

812 Contacts between ribosomal proteins (red), 18S rRNA (yellow), and the AUG codon (blue) are 813 marked. Labels refer to ribosomal proteins and elements of 18S rRNA, and to domains of the 814 IRES. Complexes assembled using the Δ dII IRES show the deleted domain marked in red. Also 815 see Table S4 for more details.

816

817 Figure S5. eIF2 related supplement, related to Figure 4.

- 818 (A) Overview of the Δ dII IRES eIF2-containing 48S initiation complex (structure $12_{\Delta dII}$).
- 819 (B-C) Presence of Domain II in the E site causes the head of the 40S subunit to open. (B) Position
- of 18S rRNA in the open ternary complex (structure 11_{wt}) (orange), *wt* IRES eIF2-containing 48S
- 821 IC (structure 12_{wt}) (yellow), and ΔdII IRES eIF2-containing 48S IC (structure $12_{\Delta dII}$) (magenta).
- 822 (C) Position of 18S rRNA in the open ternary complex (structure 11_{wt}) (orange), wt IRES w/o eIF2
- 823 48S IC (structure 13_{wt}) (yellow), and ΔdII IRES w/o eIF2 48S IC (structure $13_{\Delta dII}$) (magenta).
- 824 Measured angle between 18S rRNA h33 and h28 in the ternary complex (denoted with ') to h33 in
- 825 the *wt* IRES complex (denoted with ") shown for (C-D).
- 826 (D) Unsharpened maps for the *wt* IRES eIF2-containing 48S IC (structure 12_{wt}), left, and the ΔdII
- 827 IRES eIF2-containing 48S IC (structure $12_{\Delta dII}$), right. Comparison to canonical cap-dependent 828 initiation complexes (PDB: 6YAL) identifies the presence of eIF2 γ (cyan).
- 829 (E) The position and conformation of mRNA (magenta) and the eIF2 α -subunit for the *wt* IRES
- 830 eIF2-containing 48S IC (structure 12_{wt} , green) and the ΔdII IRES eIF2-containing 48S IC
- 831 (structure $12_{\Delta dII}$ (orange) is identical.
- (F) Maps showing that domain II occupies multiple positions in the *wt* IRES eIF2-containing 48SIC.
- 834 (G-J) Diagram of P site for the (G) IRES binary complex (structure $6_{\Delta dII}$), (H) P site for pre-48S
- 835 IC (structure 14_{wt}), (I) P site for eIF2-containing 48S IC (structure 12_{wt}), and (J) P site for eIF5B-

- 836 containing 48S IC (structure 15_{wt}). Ribosomal proteins and 18S rRNA (yellow), mRNA (red),
- tRNA (white), and eIF2 (green) are shown.
- 838

839 Figure S6, related to Figure 5.

- 840 (A) Overview of the Δ dII IRES eIF5B-containing 48S initiation complex (structure $15_{\Delta dII}$).
- 841 (B) Maps showing that domain II occupies multiple positions in the *wt* IRES eIF5B-containing
- 842 48S IC.
- 843 (C) Position of 18S rRNA in the *wt* IRES pre-48S IC (structure 14_{wt}) (orange), *wt* IRES eIF5B-
- state containing 48S IC (structure 15_{wt}) (magenta), and ΔdII IRES eIF5B-containing 48S IC (structure
- $15_{\Delta dII}$ (yellow). Measured angle between 18S rRNA h33 and h28 in the eIF5B-containing 48S IC
- 846 (denoted with ') to h33 in the pre-48S IC (denoted with ").
- (D) Global position of eIF5B bound to the intersubunit face of the 40S ribosomal subunit.
 Interactions between 18S rRNA (yellow), uS12 (salmon), and eIF1A (blue) are shown.
- (E) Coulomb potential for the GTP nucleotide in eIF5B G domain for pre-48S IC (structure 14_{wt}),
- 850 left, and 48S IC (structure 15_{wt}), right.
- (F) Comparison of conformation of switch 1 in GTP (orange) and GDP (blue), and switch 2 in
- 852 GTP (magenta) and GDP (yellow) conformations from the *C. thermophilum* G domain (grey)
- 853 (PDB: 4NCN). Conformational changes in domain II seen in the O. cuniculus 48S IC state (green)
- and the *S. cerevisiae* pre-elongation 80S state (red) (PDB: 6WOO).
- (G) Domain alignment between O. cuniculus pre-48S IC (structure 14_{wt})/48S IC (structure 15_{wt} ,
- green) and S. cerevisiae eIF5B from the pre-elongation 80S (red) (PDB: 6WOO). Position of G
- domain switch 1 (magenta) and switch 2 (orange) are marked
- 858

859 Figure S7, related to Figures 5 and 6.

- 860 (A) Structure of the O. cuniculus eIF5B G domain (PDB: 4UJD) bound to the pre-elongation 80S
- ribosome (yellow) compared to the *O. cuniculus* pre-48S IC (structure 14_{wt}, green).
- 862 (B) Structure of the O. cuniculus eIF5B G domain in the pre-48S IC (structure 14_{wt}) (green).
- 863 (C) Structure of the *C. thermophilum* eIF5B G domain (PDB: 4NCN) (blue) compared to the *O*.
- 864 *cuniculus* eIF5B G domain bound to the pre-48S IC (structure 14_{wt}) (green).
- 865 (D) Structure of the S. cerevisiae eIF5B G domain (PDB: 6WOO) bound to the pre-elongation 80S
- ribosome (red) compared to the *O. cuniculus* pre-48S IC (structure 14_{wt}) (green).

- 867 (E-F) Contacts between eS28 (salmon) and the HCV IRES (red) in the (E) pre-48S IC (structure
- 868 14_{wt}) and (F) 48S IC (structure 15_{wt}).
- 869 (G) Distance between P_{OUT} tRNA (PDB: 7A09) and the initiation codon in ternary complex
- 870 (structure 11_{wt})
- (H) Contacts between tRNA and the P site for the eIF2-containing 48S IC.
- 872
- 873 Table S1. Sample composition, related to Figure 1.
- Table S2. Data collection statistics, related to Figure 1.
- 875 **Table S3. Refinement and validation statistics, related to Figure 1.**
- 876 Table S4. Contacts between the HCV IRES and 40S subunit, related to Figure 2. Distances
- below 3.5 Å are marked as 'yes', between 3.5-4.5 Å are marked as 'weak', and above 4.5 Å marked
- 878 as 'no'.
- Table S5. Maps showing HCV IRES domain II movement, related to Figures 4 and 5.
- 880 Table S6. Contacts between eIF5B and the 40S subunit, related to Figure 5.
- Table S7. Additional maps produced during data processing, related to Figure 1 and S1.
- 882
- 883
- 884
- 885
- 886
- 887
- 888
- 889
- 890
- 891
- 892
- 893

894

895

896

897

29

- 898 STAR Methods
- 899 **Resource availability**
- 900

901 Materials availability

902 Requests for materials and additional information can be directed to Dr. Tatyana Pestova

- 903 (Tatyana.Pestova@downstate.edu;) or Dr. Joachim Frank (jf2192@cumc.columbia.edu).
- 904

905 Data availability

906 Primary models and maps (Table S3) reported in this study were deposited in the Protein 907 Data Bank (PDB) and Electron Microscopy Data Bank (EMDB) under the following accession 908 codes: structure $1_{\Delta dII}$ (PDB: XXXX; EMD-XXXX), structure $2_{\Delta dII}$ (PDB: XXXX; EMD-XXXX), 909 structure $3_{\Delta dII}$ (PDB: XXXX; EMD-XXXX), structure $4_{\Delta dII}$ (PDB: XXXX; EMD-XXXX), 910 structure $5_{\Delta dII}$ (PDB: XXXX; EMD-XXXX), structure $6_{\Delta dII}$ (PDB: XXXX; EMD-XXXX), 911 structure $7_{\Delta dII}$ (PDB: XXXX; EMD-XXXX), structure $8_{\Delta dII}$ (PDB: XXXX; EMD-XXXX), 912 structure 9_{AdII} (PDB: XXXX; EMD-XXXX), structure 10_{wt} (PDB: XXXX; EMD-XXXX), 913 structure 11_{wt} (PDB: XXXX; EMD-XXXX), structure 12_{wt} (PDB: XXXX; EMD-XXXX), 914 structure $12_{\Delta dII}$ (PDB: XXXX; EMD-XXXX), structure 13_{wt} (PDB: XXXX; EMD-XXXX), 915 structure $13_{\Delta dII}$ (PDB: XXXX; EMD-XXXX), structure 14_{wt} (PDB: XXXX; EMD-XXXX), 916 structure 15_{wt} (PDB: XXXX; EMD-XXXX), and structure 15_{Δ dII} (PDB: XXXX; EMD-XXXX). 917 For each entry half maps, the mask used for post processing, Fourier correlation curve, and local 918 resolution maps have been deposited as additional files.

919 Additional maps (table S5) showing the movement of HCV IRES domain II were deposited 920 in the EMDB under the following accession codes: structure 16_{wt} (EMD-XXXX), structure 17_{wt} 921 (EMD-XXXX), structure 18_{wt} (EMD-XXXX), structure 19_{wt} (EMD-XXXX), structure 20_{wt} 922 (EMD-XXXX), and structure 21_{wt} (EMD-XXXX), structure 22_{wt} (EMD-XXXX), structure 23_{wt} 923 (EMD-XXXX), structure 24_{wt} (EMD-XXXX), structure 25_{wt} (EMD-XXXX), structure 26_{wt} 924 (EMD-25555), structure 27_{wt} (EMD-XXXX), and structure 28_{wt} (EMD-XXXX). For each entry 925 half maps, the mask used for post processing, and Fourier correlation curve have been deposited 926 as additional files.

927 Maps obtained during data processing (Table S7) from particle stacks that were 928 compositionally and conformationally identical that were later combined were deposited in the

EMDB under the following accession codes: structure 29_{wt} (EMD-XXXX), structure 30_{wt} (EMD-XXXX), structure $31_{\Delta dII}$ (EMD-XXXX), and structure $32_{\Delta dII}$ (EMD-XXXX). For each entry half maps, the mask used for post processing, and Fourier correlation curve have been deposited as additional files.

933 Consensus maps (Table S7) that were used for focused classification were deposited in the 934 EMDB under the following accession codes: structure $33_{\Delta dII}$ (EMD-XXXX), structure $34_{\Delta dII}$ 935 (EMD-XXXX), structure 35_{wt} (EMD-XXXX), structure 36_{wt} (EMD-XXXX), structure $37_{\Delta dII}$ 936 (EMD-XXXX), structure 38_{wt} (EMD-XXXX), structure 39_{wt} (EMD-XXXX), and structure 40_{AdH} 937 (EMD-XXXX). Other high-resolution maps obtained during classification were deposited in the 938 EMDB under the following accession codes: structure 41_{wt} (EMD-XXXX), structure 42_{wt} (EMD-939 XXXX), structure 43_{wt} (EMD-XXXX), structure 44_{wt} (EMD-XXXX), structure 45_{wt} (EMD-940 XXXX), and structure $46_{\Delta dII}$ (EMD-XXXX). For each entry half maps, the mask used for post 941 processing, mask used for focused classification, and the Fourier correlation curve have been 942 deposited as additional files.

943

944 Method details

945 Plasmids

Vectors for expression of His₆-tagged eIF1A (Pestova et al., 1998a) and *Escherichia coli*methionyl tRNA synthetase (Lomakin et al., 2006) have been described. The plasmid HCVMSTN-Stop (Hashem et al., 2013) containing HCV Type 1 nt. 40–375 was used for transcription
of mRNA containing the *wt* HCV IRES. A derivative for transcription of HCV IRES lacking
domain II (containing HCV nt. 125-375) was made by GenScript Corp. (Piscataway, NJ). The
HCV plasmids were linearized by BamHI, and mRNAs were transcribed using T7 RNA
polymerase (Thermo Scientific).

953

954 Purification of factors, ribosomal subunits and aminoacylation of tRNA

Native mammalian 40S subunits, eIF2, eIF3 and eIF5B were purified from rabbit
reticulocyte lysate (RRL) (Green Hectares), as described (Pisarev et al., 2007). Recombinant
eIF1A and *Escherichia coli* methionyl tRNA synthetase were expressed and purified from *E. coli* as described (Pisarev et al., 2007).

959 For purification of native rabbit total tRNA, 200 ml RRL were centrifuged at 45,000 rpm 960 for 4.5 h in a Beckman 50.2 Ti rotor at 4°C in order to pellet polysomes. The supernatant was 961 dialyzed overnight against buffer A (20 mM Tris [pH 7.5], 4 mM MgCl₂, 250 mM KCl, 2 mM 962 DTT) and applied to a DE52 (Whatman) column equilibrated with buffer A. The tRNA was eluted 963 with buffer B (20 mM Tris [pH 7.5], 3 mM MgCl₂, 700 mM NaCl, 2 mM DTT) and precipitated 964 overnight with 2.5 volumes of ethanol at -80°C. The precipitate was centrifuged at 13,000 rpm for 965 15 minutes and resuspended in 5 ml buffer C (100 mM Tris [pH 7.5], 5 mM MgCl₂), phenol-966 chloroform (pH 4.7)) extracted and precipitated again with 0.3 M NaOAc and 2.5 volumes of 967 ethanol. To isolate tRNA, the pellet was dissolved and subjected to gel filtration on a Superdex 75 968 column (Pestova and Hellen, 2001). Purified total tRNA was aminoacylated using E. coli methionyl tRNA synthetase (to obtain Met-tRNA^{i,Met}) as described (Pisarev et al., 2007). 969

970

971 Assembly of ribosomal complexes

To form 48S initiation complexes, 7 pmol HCV IRES mRNA (*wt* or Δ domain II mutant) were incubated with 3.5 pmol 40S subunits, 10 pmol eIF1A, 4.5 pmol eIF3, total native rabbit tRNA containing 3.5 pmol Met-tRNA_i^{Met}, and 6 pmol eIF2 or 10 pmol eIF5B in 40 µl buffer D (20 mM Tris [pH 7.5], 100 mM KAc, 2.5 mM MgCl₂, 2 mM DTT, 0.25 mM spermidine, 1 mM ATP and 0.2 mM GTP) for 10 minutes at 37°C. The obtained complexes (containing 87.5 nM 40S subunits) were applied directly onto grids without dilution.

978

979 Grid preparation and electron microscopy

980 Gold foil grids were prepared from Quantifoil gold mesh grids (Passmore and Russo, 981 2016). Initially, Quantifoil R0.6/1.0 300 mesh gold grids (Quantifoil Micro Tools GmbH) were 982 visually inspected to check for uniformity and intactness of the Quantifoil layer and then placed 983 into an Auto 306 Turbo Vacuum Coater (Edwards Vacuum) at a pressure of 10³ Pa and then gold 984 wire (Ted Pella, Inc) was evaporated for approximately 8 minutes to create a 500 Å layer. 985 Deposition thickness was determined using the inbuilt film thickness monitor. To remove the 986 underlying Quantifoil carbon foil layer the grids were then treated with plasma using a Gatan 987 Solarus 950 (Gatan Inc) operated at 25 W for 4 minutes with an argon/oxygen gas mixture.

To prepare hydrophilic grids, 30 minutes prior to sample application, grids were treated with plasma using a Gatan Solarus 950 (Gatan Inc) operated at 25W for 25 seconds with a 990 hydrogen/oxygen gas mixture. These grids were then transferred to the environmental chamber of 991 a Vitrobot Mark IV (Thermo Fisher Scientific) maintained at 4°C and 100% humidity. Here 3 μ L 992 of sample were applied and then blotted for 4 seconds with blot force 3 before immediate plunging 993 into an a cooled (77K) ethane-propane mixture (Tivol et al., 2008) and then transferred to liquid 994 nitrogen. Selected grids were screened to confirm sample composition and ice thickness using a 995 Tecnai F20 electron microscope (Thermo Fisher Scientific) equipped with a field emission gun 996 (FEG) operating at 200kV and a K2 summit direct electron detector (Gatan, Inc).

997 After screening grids from each sample, data collection was performed on a Tecnai Polara 998 F30 (Thermo Fisher Scientific) equipped with an FEG operating at 300 kV and a K3 direct electron 999 detector (Gatan, Inc). Movies were collected at a nominal magnification of 52,000× and defocus 1000 range of -0.5 to -2.5 µm in counting mode with a pixel size of 0.95 Å/pixel using the automated 1001 collection software Leginon (Potter et al., 1999; Carragher et al., 2000; Suloway et al., 2005). Each movie consisted of 40 frames recorded over 4 seconds with a total dose of 70.9 e^{-/A^2} . Due to 1002 sample conditions the 40S ribosome may enter a preferred orientation and so potions of the data 1003 were collected with a 30° stage tilt (Table S2). For the wt IRES eIF2-containing sample 14,815 1004 micrographs (14,815 at 30° stage tilt) were collected over 2 sessions, for the wt IRES eIF5B-1005 1006 containing sample 27,263 micrographs (20,509 at 30° stage tilt) were collected over 4 sessions, for the Δ dII IRES eIF2-containing sample 22,735 micrographs (17,695 at 30° stage tilt) were 1007 1008 collected over 3 sessions, and for the Δ dII IRES eIF5B-containing sample 13,809 micrographs 1009 (13,809 at 30° stage tilt) were collected over 2 sessions (Table S2). Optical groups of micrographs 1010 with similar beam tilt values were identified using k-means clustering on the image shift values 1011 recorded by the microscope during data collection.

1012

1013 Image processing

Gain references for each session were produced by visually screening ~1000 micrographs to remove images that contained gold foil and then summing them using cisTEM *sum_all_tifs* (Grant et al., 2018). Movies were then aligned using MotionCor2 (Zheng et al., 2017) with dose weighting of 1.77 e⁻/Å²/frame and local patch correction with 8×5 patches. Initial CTF parameters were estimated using CTFFIND4 (Rohou and Grigorieff, 2015). Particle locations were identified using Topaz version 0.2.3 (Bepler et al. 2019) by initially downscaling all micrographs by 8× and then using the Topaz general model to identify particles. Particles with a confidence score below

1021 0 were removed and the remaining positions rescaled for subsequent processing in Relion 3.1
1022 (Scheres, 2012; 2016; Zivanov et al., 2018; 2019).

1023 Initially, we identified 2,183,185 particles for the wt IRES eIF2-containing sample (147 particles per micrograph), 1,133,335 particles for the wt IRES eIF5B-containing sample 1024 1025 (42 particles per micrograph), 2,213,826 particles for the ΔdII IRES eIF2-containing sample (97 particles per micrograph), and 1,459,506 particles for the Δ dII IRES eIF5B-containing sample 1026 1027 (106 particles per micrograph). Particle locations were extracted from micrographs into 1028 downsampled boxes of 100×100 pixels (at 3.8 Å/pixel) to speed initial classification. This 1029 corresponds to 400×400-pixel boxes (at 0.95 Å/pixel) without downsampling. 25 iterations of 2D 1030 classification were performed to identify incorrectly picked particles, contamination, and other 1031 particles that were unable to be correctly aligned (e.g., due to poor SNR). Particles that were 1032 selected for removal were subjected to additional 2D classification to confirm that they did not 1033 contain clear 40S ribosome particles.

1034 After initial screening of the 2D classification data the remaining particles for each sample 1035 were 1.201.923 particles for the *wt* IRES eIF2-containing sample (81 particles per micrograph), 1036 736,700 particles for the wt IRES eIF5B-containing sample (36 particles per micrograph), 1,484,658 particles for the Δ dII IRES eIF2-containing sample (84 particles per micrograph), and 1037 1038 1,119,610 particles for the AdII IRES eIF5B-containing sample (81 particles per micrograph). For 1039 each sample, all particles were refined into a single model which was used to estimate the defocus 1040 values on a per-particle basis, followed by an additional refinement step, and then 3D classification 1041 without alignment into 10 classes for 25 iterations. This initial 3D classification was used to 1042 identify the major conformational states present in each sample, as well as further removal of poor-1043 quality particles. For the wt IRES eIF2-containing sample we identified 580,938 particles in the 1044 closed state, 176,793 particles in the open sate, and removed 444,192 particles. For the wt IRES 1045 eIF5B-containing sample we identified 378,325 open state, 360,338 closed state, and removed 1046 58,037 particles. For the Δ dII IRES eIF5B-containing sample we identified 883,893 particles in 1047 the closed state, and removed 62,455 particles. For the ΔdII IRES eIF2-containing sample we 1048 identified 615,125 particles in the closed state, 198,920 particles in the intermediate-open state, 1049 and removed 670,433 particles. All particles that were selected for removal were subjected to 1050 additional 2D classification and 3D refinement steps to confirm that they did not contain 40S 1051 ribosome complexes.

1052

1053 General processing pathway

1054 All particles were re-extracted at full-size (400×400-pixel box, 0.95 Å/pixel) and 1055 underwent iterations of 3D refinement, following by anisotropic magnification correction, defocus 1056 refinement, and beam tilt estimation. Multiple rounds of 3D classification (25 iterations, without alignment) were used to progressively remove poor quality particles. After each round of CTF 1057 1058 refinement each particle stack underwent 3D refinement and was checked for increase in resolution 1059 and visual improvement of map density. Once CTF refinement no longer improved map quality, 1060 particle polishing using all frames was performed and then iterations of CTF refinement as outline above were completed. Focused classification on consensus maps was performed to isolate desired 1061 conformational or compositional states (see below). 1062

1063

1064 wt IRES eIF2-containing sample

1065 After 3D classification the consensus map of closed 40S ribosome particles (Table S7) from the wt IRES eIF2-containing sample contained 530,720 particles at 3.1 Å resolution (structure 1066 36_{wt} ; EMD-XXXX) underwent focused classification by enclosing Met-tRNA_i^{Met} and the eIF2 α 1067 subunit in a mask. Iterations of focused classification were able to produce two high quality classes 1068 of either the eIF2-containg 48S IC with 46,904 particles at 3.6 Å resolution (structure 12_{wt} ; 1069 1070 PDB: XXXX; EMD-XXXX) and the 48S IC w/o eIF2 with 15,598 particles at 4.4 Å resolution 1071 (structure 13wt; PDB: XXXX; EMD-XXXX). An additional class of the eIF2-containg 48S IC lacking eIF1A with 45,571 particles at 3.6 Å resolution (structure 45_{wt}; EMD-XXXX) was 1072 1073 obtained. Extensive classification of the remaining 422,647 particles produced maps that showed the 40S ribosome bound to eIF2 and/or Met-tRNA_i^{Met} but with a low resolution, or the ribosome 1074 1075 lacking both factors.

1076 To determine the positions that IRES domain II occupies the region around domain II was 1077 masked and classified into 10 classes over 25 iterations without alignment. Six classes were able 1078 to be clearly resolved showing IRES domain II sampling different positions around the ribosome 1079 head. Class 1 containing 41,393 particles at 3.8 Å resolution (structure 16_{wt} ; EMD-XXXX), class 1080 2 containing 39,148 particles at 3.8 Å resolution (structure 17_{wt} ; EMD-XXXX), class 3 containing 1081 49,034 particles at 3.7 Å resolution (structure 18_{wt} ; EMD-XXXX), class 4 containing 66,090 1082 particles at 3.6 Å resolution (structure 19_{wt} ; EMD-XXXX), class 5 containing 24,190 particles at 10833.9 Å resolution (structure 20_{wt} ; EMD-XXXX), and class 6 containing 36,155 particles at 3.8 Å1084resolution (structure 21_{wt} ; EMD-XXXX). Extensive classification of the remaining 274,7101085particles could not further resolved additional positions of domain II.

After extracting at full size the consensus map of the open 40S ribosome particles (Table S7) from the *wt* IRES eIF2-containing sample contained 176,793 particles at 3.8 Å resolution (structure 29_{wt}; EMD-XXXX).

1089

1090 wt IRES eIF5-containing sample

1091 The consensus map of closed 40S ribosome particles (Table S7) from the wt IRES eIF5Bcontaining sample contained 360.338 particles at 3.4 Å resolution (structure 39_{wt}; EMD-XXXX) 1092 1093 underwent focused classification by enclosing eIF5B in a mask. This could be classified into three 1094 high-resolution classes of the eIF5B-containing 48S IC eIF5B: one containing 133,782 particles 1095 at 3.7 Å resolution (structure 15_{wt}; PDB: XXXX; EMD-XXXX), one containing 109,025 particles 1096 at 3.7 Å resolution (structure 41_{wt}; EMD-XXXX), and one containing 55,367 at 3.8 Å resolution (structure 42_{wt}; EMD-XXXX). The remaining 62,164 particles showed the 48S IC at 3.9 Å 1097 1098 resolution but the occupancy of eIF5B was lower (structure 43_{wt}; EMD-XXXX).

1099 To determine the positions that IRES domain II occupies the region around domain II was 1100 masked and classified into 10 classes over 25 iterations without alignment. Seven classes were 1101 able to be resolved showing IRES domain II sampling different positions around the ribosome 1102 head. Class 1 containing 20,138 particles at 5.0 Å resolution (structure 22_{wt}; EMD-XXXX), class 1103 2 containing 11,082 particles at 5.4 Å resolution (structure 23_{wt}; EMD-XXXX), class 3 containing 1104 16,584 particles at 5.2 Å resolution (structure 24_{wt}; EMD-XXXX), class 4 containing 16,217 1105 particles at 4.9 Å resolution (structure 25_{wt}; EMD-XXXX), class 5 containing 8,102 particles at 1106 6.0 Å resolution (structure 26_{wt}; EMD-XXXX), class 6 containing 13,152 particles at 5.3 Å 1107 resolution (structure 27_{wt}; EMD-XXXX), and class 7 containing 7,029 particles at 6.2 Å resolution 1108 (structure 28_{wt}; EMD-XXXX). Extensive classification of the remaining 268,034 particles could 1109 not further resolved the position of domain II.

1110 The consensus map of open 40S ribosome particles (Table S7) from the *wt* IRES eIF5B-1111 containing sample was classified into two classes: a consensus eIF5B-containing pre-48S IC with 1112 199,047 particles at 3.6 Å (structure 38_{wt} ; EMD-XXXX) and the open binary complex with 1113 147,309 particles at 4.1 Å resolution (structure 30_{wt} ; EMD-XXXX). The 31,969 remaining

1114 particles were subjected to 3D classification but did now contain high-quality classes. The 1115 consensus map of the eIF5B containing pre-48S IC (structure 38_{wt}) was masked around eIF5B and 1116 focused classification produced two classes, one with 60,578 particles at 3.8 Å (structure 14_{wt} ; 1117 PDB: XXXX; EMD-XXXX), and a lower-resolution map from 29,072 particles at 4.2 Å (structure 1118 44_{wt}; EMD-XXXX).

1119

1120 **AdII IRES eIF2-containing sample**

1121 The consensus map of closed 40S ribosome particles (Table S7) from the Δ dII IRES eIF2containing sample contained 615,195 particles at 3.3 Å resolution (structure 37_{AdII}; EMD-25596) 1122 underwent focused classification by enclosing Met-tRNA_i^{Met} and the eIF2 α subunit in a mask. 1123 1124 Iterations of focused classification were able to produce two high quality classes of either the eIF2-1125 containg 48S IC (structure $12_{\Delta dII}$; PDB: XXXX; EMD-XXXX), and the 48S IC w/o eIF2 (structure 1126 13_{Adll}; PDB: XXXX; EMD-XXXX). An additional class of 147,713 particles at 3.6 Å (structure $46_{\Delta dII}$; EMD-XXXX) showed the 48S IC but with very poor density for eIF2. Extensive 1127 1128 classification of the remaining 348,071 particles did not produced any high-quality maps. The 1129 consensus map of the intermediate conformation 40S ribosome particles (Table S7) from the ΔdII IRES eIF2-containing sample had 198,920 particles at 3.5 Å resolution (structure 31_{AdII}; EMD-1130 1131 25590).

1132

1133 **AdII IRES eIF5B-containing sample**

1134 3D classification of the closed state eIF5B-containing 40S ribosome produced three classes 1135 that were processed further (Figure S1G; Table S7). The consensus map of closed 40S ribosome 1136 particles (Table S7) from the ∆dII IRES eIF5B-containing sample contained 148,763 particles at 1137 3.4 Å resolution (structure $40_{\Delta dII}$; EMD-XXXX) and underwent focused classification by enclosing eIF5B in a mask. Iterations of focused classification were able to produce one high 1138 1139 quality class of the eIF5B-containg 48S IC (structure $15_{\Delta dII}$; PDB: XXXX; EMD-XXXX). Classification of the remaining 99,239 particles produced maps at either low resolution or lacking 1140 1141 eIF5B. The consensus map showing the closed 40S ribosome with multiple HCV IRES states 1142 (Table S7) had 346,516 particles at 3.6 Å resolution (structure 33_{AdII}; EMD-XXXX). A mask was 1143 prepared around IRES domains S1/S2/IIIe/IIIf and focused classification resolved six classes of 1144 the IRES in various association/dissociation states: (1) the early stage association between the

1145 IRES and 40S/IRES_{Δ dII} binary complex with 42,271 particles at 4.3 Å resolution (structure 1_{Δ dII; 1146 PDB: XXXX; EMD-XXXX), (2) the early stage association between the IRES and 40S/IRES_{AdII} 1147 binary complex with 28,684 particles at 4.6 Å resolution (structure $2_{\Delta dII}$; PDB: 7SYH; EMD-XXXX), (3) the early stage association between the IRES and $40S/IRES_{\Delta dII}$ binary complex with 1148 1149 24,545 particles at 4.5 Å resolution (structure $3_{\Delta dII}$; PDB: XXXX; EMD-XXXX), (4) the early 1150 stage association between the IRES and $40S/IRES_{\Delta dII}$ binary complex with 27,043 particles at 4.8 1151 Å resolution (structure $4_{\Delta dII}$; PDB: XXXX; EMD-XXXX), (5) the early stage association between the IRES and 40S/IRES_{AdII} binary complex with 48,757 particles at 4.2 Å resolution (structure 1152 1153 $5_{\Delta dII}$; PDB: XXXX; EMD-XXXX), and (6) the canonically bound IRES 40S/IRES_{AdII} binary complex with 29,657 particles at 4.5 Å resolution (structure 6_{AdII} ; PDB: XXXX; EMD-XXXX). 1154 1155 The remaining 145,559 particles were classified into either low-resolution maps or with the 40S ribosome lacking the HCV IRES. The consensus map of the intermediate 40S ribosome particles 1156 1157 (Table S7) from the Δ dII IRES eIF5B-containing sample had 287,087 particles at 4.5 Å resolution (structure $32_{\Delta dII}$; EMD-XXXX). 1158

1159

1160 Combining ΔdII IRES intermediate 40S ribosome particles and focused classification

Both eIF2-, and eIF5B-containing samples prepared on the AdII IRES yielded 1161 1162 classes that showed the HCV IRES bound to the 40S ribosome where the head of the ribosome was in multiple states (structure $31_{\Delta dII}$ - $32_{\Delta dII}$). Both maps were visually inspected and showed high 1163 1164 similarity (unsharpened maps a correlation of 0.9834, and after B-factor sharpening 0.9295). We 1165 combined these particles into a consensus map of 456,311 particles at 3.5 Å resolution (structure 1166 $34_{\Delta dII}$; EMD-XXXX) that underwent focused classification of the entire head region of the ribosome that produced three classes: the closed 40S/IRES_{AdII} binary complex with 59,660 1167 1168 particles at 4.8 Å resolution (structure $7_{\Delta dII}$; PDB: XXXX; EMD-XXXX), the intermediate-open 40S/IRES_{$\Delta dII}$ binary complex with 144,252 particles at 4.0 Å resolution (structure $8_{\Delta dII}$;</sub> 1169 1170 PDB: XXXX; EMD-XXXX), and the open $40S/IRES_{AdII}$ binary complex with 46,095 particles at 1171 4.6 Å resolution (structure 9_{AdII}; PDB: XXXX; EMD-XXXX). The remaining 206,304 particles 1172 were classified into low resolution maps.

1173

1174 Combining wt IRES open 40S ribosome particles and focused classification

1175 Both eIF2-, and eIF5B-containing samples prepared on the wt IRES yielded classes that 1176 showed the HCV IRES bound to the 40S ribosome with IRES domain II inserted into the E site 1177 (structure 29_{wt}-30_{wt}). Both maps were visually inspected and showed high similarity (unsharpened maps correlation of 0.9945, and after B-factor sharpening 0.9464). We combined these particles 1178 1179 into a consensus map of 324,102 particles at 3.3 Å resolution (structure 35_{wt}; EMD- XXXX) that 1180 underwent focused classification of eIF1A that produced two classes: the binary complex with 1181 119,320 particles at 3.8 Å resolution (structure 10_{wt}; PDB: XXXX; EMD-XXXX), and the ternary 1182 complex with 204,782 particles at 3.8 Å resolution (structure 11_{wt}; PDB: XXXX; EMD-XXXX). 1183

1184

84 Model building, and refinement

1185 For all data, where applicable, we were able to unambiguously fit the head and body of the 1186 40S (PDB: 6D9J; Pisareva et al. 2018), HCV IRES (PDB: 5FLX; Yamamoto et al. 2015), eIF1A 1187 (PDB: 4KZZ; Lomakin and Steitz 2013), tRNA (PDB: 5K0Y; Simonetti et al. 2016) eIF2a subunit 1188 (PDB: 6085; Kenner et al. 2019), and eIF5B (PDB: 4UJD; Yamamoto et al. 2014). Initial model 1189 fitting was performed using UCSF Chimera v1.14 (Pettersen et al., 2004) with additional 1190 modelling in Coot (Emsley and Cowtan, 2004). For regions of eIF5B that did not have available models (e.g., Switch 1) model building was performed independently and then cross-checked for 1191 1192 consistency. All models underwent one round of Phenix geometry minimization and multiple 1193 rounds of PHENIX real-space refinement (Adams et al., 2010; Afonine et al., 2018).

- 1194
- 1195 Figures

1196

All figures were prepared using UCSF Chimera v1.14 (Pettersen et al., 2004).

1197

1198 **Quantification and statistical analysis**

Global resolution estimates were calculated using the 0.143 FSC criterion (Rosenthal and Henderson, 2003). Local resolution maps were calculated using Relion 3.1 (Scheres, 2012; 2016; Zivanov et al., 2018; 2019) using the B-factor determined during post processing and the Modulation transfer function (MTF) curve for the K3 camera at 300 kV provided by the manufacturer. (<u>https://www.gatan.com/techniques/cryo-em#MTF</u>). RMSD calculations for 18S rRNA chains were performed using Pymol (Schrödinger, 2015). Model validation for all models

- 1205 were calculated using PHENIX (Adams et al., 2010; Afonine et al., 2018) installed as part of the
- 1206 SBGrid package (Morin et al., 2013).

1207

1208

1209 REFERENCES

| 1 | 2 | 1 | 0 |
|---|---|---|---|
| | _ | | 0 |

- Acker, M.G., Shin, B.S., Dever, T.E., and Lorsch, J.R. (2006). Interaction between eukaryotic initiation factors 1A and 5B is required for efficient ribosomal subunit joining. J. Biol. Chem. 281, 8469-8475. 10.1074/jbc.M600210200.
- $1212 \qquad \text{and } 35 \text{ is required for efficient hoosonial subunit joining. J. Biol. Chem. 281, 8409-6475. 10.1074/jbc.10000210200.}$
- 1214 Adams, P.D., Afonine, P.V., Bunkóczi, G., Chen, V.B., Davis, I.W., Echols, N., Headd, J.J., Hung, L.W., Kapral, G.J.,
- 1215 Grosse-Kunstleve, R.W., McCoy, A.J., Moriarty, N.W., Oeffner, R., Read, R.J., Richardson, D.C., Richardson, J.S.,
- 1216 Terwilliger, T.C., Zwart, P.H. (2010). PHENIX: a comprehensive Python-based system for macromolecular structure
- 1217 solution. Acta Crystallogr. D Biol. Crystallogr. 66, 213–221. <u>10.1107/S0907444909052925</u>.
- 1218
- Afonine, P.V., Poon, B.K., Read, R.J., Sobolev, O.V., Terwilliger, T.C., Urzhumtsev, A., and Adams, P.D. (2018).
 Real-space refinement in PHENIX for cryo-EM and crystallography. Acta Crystallogr. D Struct. Biol. 74, 531-544.
 10.1107/S2059798318006551.
- 1222

Angulo, J., Ulryck, N., Deforges, J., Chamond, N., Lopez-Lastra, M., Masquida, B., and Sargueil, B. (2016). LOOP
IIId of the HCV IRES is essential for the structural rearrangement of the 40S-HCV IRES complex. Nucleic Acids Res.
44, 1309-25. 10.1093/nar/gkv1325.

- 1226
- Arhab, Y., Bulakhov, A.G., Pestova, T.V., and Hellen, C.U.T. (2020). Dissemination of internal ribosomal entry sites
 (IRES) between viruses by horizontal gene transfer. Viruses 12, 612. <u>10.3390/v12060612</u>.
- 1229
- Battiste, J.L., Pestova, T.V., Hellen, C.U., and Wagner, G. (2000). The eIF1A solution structure reveals a large RNAbinding surface important for scanning function. Mol. Cell 5, 109-119. <u>10.1016/s1097-2765(00)80407-4</u>
- 1232
- Bepler, T., Morin, A., Rapp, M., Brasch, J., Shapiro, L., Noble, A.J., and Berger, B. (2019). Positive-unlabeled
 convolutional neural networks for particle picking in cryo-electron micrographs. Nat. Methods 16, 1153-1160.
 10.1038/s41592-019-0575-8.
- 1236
- Boehringer, D., Thermann, R., Ostareck-Lederer, A., Lewis, J.D., and Stark, H. (2005). Structure of the hepatitis C
 virus IRES bound to the human 80S ribosome: remodeling of the HCV IRES. Structure 13, 1695-706.
 10.1016/j.str.2005.08.008.
- 1240
- 1241 Brito Querido, J., Sokabe, M., Kraatz, S., Gordiyenko, Y., Skehel, J.M., Fraser, C.S., and Ramakrishnan, V. (2020).
- 1242 Structure of a human 48S translational initiation complex. Science 369, 1220-1227. 10.1126/science.aba4904.
- 1243

| 1244 | Carragher, B., Kisseberth, N., Kriegman, D., Milligan, R.A., Potter, C.S., Pulokas, J., and Reilein, A. (2000). Leginon: |
|----------------------|---|
| 1245 | an automated system for acquisition of images from vitreous ice specimens. J. Struct. Biol. 132, 33-45. |
| 1246 | 10.1006/jsbi.2000.4314. |
| 1247 | |
| 1248 | de Breyne, S., Yu, Y., Pestova, T.V., and Hellen, C.U. (2008). Factor requirements for translation initiation on the |
| 1249 | Simian picornavirus internal ribosomal entry site. RNA 14, 367-380. 10.1261/rna.696508. |
| 1250 | |
| 1251 | des Georges, A., Dhote, V., Kuhn, L., Hellen, C.U., Pestova, T.V., Frank, J., and Hashem, Y. (2015) Structure of |
| 1252 | mammalian eIF3 in the context of the 43S preinitiation complex. Nature 525, 491-495. 10.1038/nature14891. |
| 1253 | |
| 1254 | d'Imprima, E., Floris, D., Joppe, M., Sánchez, R., Grininger, M., and Kühlbrandt, W. (2019). Protein denaturation at |
| 1255 | the air-water interface and how to prevent it. Elife 8, e42747. 10.7554/eLife.42747. |
| 1256 | |
| 1257 | Easton, L.E., Locker, N., and Lukavsky, P.J. (2009). Conserved functional domains and a novel tertiary interaction |
| 1258 | near the pseudoknot drive translational activity of hepatitis C virus and hepatitis C virus-like internal ribosomal entry |
| 1259 | sites. Nucleic Acids Res. 37, 5537-5549. 10.1093/nar/gkp588. |
| 1260 | |
| 1261 | Emsley, P., and Cowtan, K. (2004). Coot: model-building tools for molecular graphics. Acta Crystallogr. D Biol. |
| 1262 | Crystallogr. 60, 2126-2132. 10.1107/S0907444904019158. |
| 1263 | |
| 1264 | Filbin, M.E., and Kieft, J.S. (2011). HCV IRES domain IIb affects the configuration of coding RNA in the 40S |
| 1265 | subunit's decoding groove. RNA 17, 1258-1273. 10.1261/rna.2594011. |
| 1266 | |
| 1267 | Fletcher, C.M., Pestova, T.V., Hellen, C.U., and Wagner, G. (1999). Structure and interactions of the translation |
| 1268 | initiation factor eIF1. EMBO J. 18, 2631-2637. <u>10.1093/emboj/18.9.2631</u> . |
| 1269 | |
| 1270 | Glaeser, R.M. (2021). Preparing better samples for cryo-electron microscopy: Biochemical challenges do not end with |
| 1271 | isolation and purification. Annu. Rev. Biochem. 90, 451-474. 10.1146/annurev-biochem-072020-020231 |
| 1272 | |
| 1273 1274 1275 | Grant, T., Rohou, A., and Grigorieff, N. (2018). <i>cis</i> TEM, user-friendly software for single-particle image processing. Elife 7, e35383. <u>10.7554/eLife.35383</u> . |
| 1276 | Hashem, Y., des Georges, A., Dhote, V., Langlois, R., Liao, H.Y., Grassucci, R.A., Pestova, T.V., Hellen, C.U., and |
| 1277 | Frank, J. (2013). Hepatitis-C-virus-like internal ribosome entry sites displace eIF3 to gain access to the 40S subunit. |
| 1278 | Nature 503, 539-543. 10.1038/nature12658. |
| 1279 | |

| 1280 | Honda, M., Ping, L.H., Rijnbrand, R.C., Amphlett, E., Clarke, B., Rowlands, D., and Lemon, S.M. (1996). Structural |
|------|---|
| 1281 | requirements for initiation of translation by internal ribosome entry within genome-length hepatitis C virus RNA. |
| 1282 | Virology 222, 31-42. 10.1006/viro.1996.0395. |
| 1283 | |
| 1284 | Huang, B.Y., and Fernández, I.S. (2020). Long-range interdomain communications in eIF5B regulate GTP hydrolysis |
| 1285 | and translation initiation. Proc. Natl. Acad. Sci. U.S.A. 117, 1429-1437. 10.1073/pnas.1916436117. |
| 1286 | |
| 1287 | Hussain, T., Llácer, J.L., Fernández, I.S., Munoz, A., Martin-Marcos, P., Savva, C.G., Lorsch, J.R., Hinnebusch, A.G., |
| 1288 | and Ramakrishnan, V. (2014). Structural changes enable start codon recognition by the eukaryotic translation initiation |
| 1289 | complex. Cell 159, 597-607. 10.1016/j.cell.2014.10.001. |
| 1290 | |
| 1291 | Hussain, T., Llácer, J.L., Wimberly, B.T., Kieft, J.S., and Ramakrishnan, V. (2016). Large-Scale Movements of IF3 |
| 1292 | and tRNA during Bacterial Translation Initiation. Cell 167, 133-144.e13. 10.1016/j.cell.2016.08.074. |
| 1293 | |
| 1294 | Jaafar, Z.A., Oguro, A., Nakamura, Y., and Kieft, J.S. (2016). Translation initiation by the hepatitis C virus IRES |
| 1295 | requires eIF1A and ribosomal complex remodeling. Elife 5, e21198. 10.7554/eLife.21198. |
| 1296 | |
| 1297 | Jackson, R.J., Hellen, C.U., and Pestova, T.V. (2010). The mechanism of eukaryotic translation initiation and |
| 1298 | principles of its regulation. Nat. Rev. Mol. Cell. Biol. 11, 113-127. 10.1038/nrm2838. |
| 1299 | |
| 1300 | Ji, H., Fraser, C.S., Yu, Y., Leary, J., and Doudna, J.A. (2004). Coordinated assembly of human translation initiation |
| 1301 | complexes by the hepatitis C virus internal ribosome entry site RNA. Proc. Natl. Acad. Sci. U.S.A. 101, 16990-16995. |
| 1302 | 10.1073/pnas.0407402101. |
| 1303 | |
| 1304 | Jumper, J., Evans, R., Pritzel, A., Green, T., Figurnov, M., Ronneberger, O., Tunyasuvunakool, K., Bates, R., Žídek, |
| 1305 | A., Potapenko, A., Bridgland, A., Meyer, C., Kohl, S.A.A., Ballard, A.J., Cowie, A., Romera-Paredes, B., Nikolov, |
| 1306 | S., Jain, R., Adler, J., Back, T., Petersen, S., Reiman, D., Clancy, E., Zielinski, M., Steinegger, M., Pacholska, M., |
| 1307 | Berghammer, T., Bodenstein, S., Silver, D., Vinyals, O., Senior, A.W., Kavukcuoglu, K., Kohli, P., Hassabis, D. |
| 1308 | (2021). Highly accurate protein structure prediction with AlphaFold. Nature 596, 583-589. 10.1038/s41586-021- |
| 1309 | 03819-2. |
| 1310 | |
| 1311 | Kenner, L.R., Anand, A.A., Nguyen, H.C., Myasnikov, A.G., Klose, C.J., McGeever, L.A., Tsai, J.C., Miller-Vedam, |
| 1312 | L.E., Walter, P., and Frost, A. (2019). eIF2B-catalyzed nucleotide exchange and phosphoregulation by the integrated |
| 1313 | stress response. Science 364, 491-495. 10.1126/science.aaw2922. |
| 1314 | |
| 1315 | Kieft, J.S., Zhou, K., Jubin, R., and Doudna, J.A. (2001). Mechanism of ribosome recruitment by hepatitis C IRES |

1316 RNA. RNA 7, 194-206. 10.1017/s1355838201001790.

| 1017 | |
|------|---|
| 1317 | |
| 1318 | Kolupaeva, V.G., Pestova, T.V., and Hellen, C.U. (2000). An enzymatic footprinting analysis of the interaction of |
| 1319 | 40S ribosomal subunits with the internal ribosomal entry site of hepatitis C virus. J Virol. 2000 Jul;74(14):6242-50. |
| 1320 | 10.1128/jvi.74.14.6242-6250.2000. |
| 1321 | |
| 1322 | Kratzat, H., Mackens-Kiani, T., Ameismeier, M., Potocnjak, M., Cheng, J., Dacheux, E., Namane, A., Berninghausen, |
| 1323 | O., Herzog, F., Fromont-Racine, M., Becker, T., and Beckmann, R. (2021). A structural inventory of native ribosomal |
| 1324 | ABCE1-43S pre-initiation complexes. EMBO J. 40, e105179. <u>10.15252/embj.2020105179</u> . |
| 1325 | |
| 1326 | Kuhle, B., and Ficner, R. (2014). eIF5B employs a novel domain release mechanism to catalyze ribosomal subunit |
| 1327 | joining. EMBO J. 33, 1177-1191. 10.1002/embj.201387344. |
| 1328 | |
| 1329 | Llácer, J.L., Hussain, T., Marler, L., Aitken, C.E., Thakur, A., Lorsch, J.R., Hinnebusch, A.G., and Ramakrishnan, V. |
| 1330 | (2015). Conformational Differences between Open and Closed States of the Eukaryotic Translation Initiation |
| 1331 | Complex. Mol. Cell 59, 399-412. 10.1016/j.molcel.2015.06.033. |
| 1332 | |
| 1333 | Locker, N., Easton, L.E., and Lukavsky, P.J. (2007). HCV and CSFV IRES domain II mediate eIF2 release during |
| 1334 | 80S ribosome assembly. EMBO J. 26, 795-805. 10.1038/sj.emboj.7601549. |
| 1335 | |
| 1336 | Lomakin, I.B., and Steitz, T.A. (2013). The initiation of mammalian protein synthesis and mRNA scanning |
| 1337 | mechanism. Nature 500, 307-311. 10.1038/nature12355. |
| 1338 | |
| 1339 | Lomakin, I.B., Shirokikh, N.E., Yusupov, M.M., Hellen, C.U., and Pestova, T.V. (2006). The fidelity of translation |
| 1340 | initiation: reciprocal activities of eIF1, IF3 and YciH. EMBO J. 25, 196-210. 10.1038/sj.emboj.7600904. |
| 1341 | |
| 1342 | Maag, D., Fekete, C.A., Gryczynski, Z., and Lorsch, J.R. (2005). A conformational change in the eukaryotic |
| 1343 | translation preinitiation complex and release of eIF1 signal recognition of the start codon. Mol. Cell 17, 265-275 |
| 1344 | 10.1016/j.molcel.2004.11. |
| 1345 | |
| 1346 | Malygin, A.A., Kossinova, O.A., Shatsky, I.N., and Karpova, G.G. (2013a). HCV IRES interacts with the 18S rRNA |
| 1347 | to activate the 40S ribosome for subsequent steps of translation initiation. Nucleic Acids Res. 41, 8706-8714. |
| 1348 | 10.1093/nar/gkt632. |
| 1349 | |
| 1350 | Malygin, A.A., Shatsky, I.N., and Karpova, G.G. (2013b). Proteins of the human 40S ribosomal subunit involved in |
| 1351 | hepatitis C IRES binding as revealed from fluorescent labeling. Biochemistry (Mosc). 78, 53-59. |
| 1352 | 10.1134/S0006297913010069. |
| 1353 | |

| 1354 | Marintchev, A., Kolupaeva, V.G., Pestova, T.V., and Wagner, G. (2003). Mapping the binding interface between |
|------|--|
| 1355 | human eukaryotic initiation factors 1A and 5B: a new interaction between old partners. Proc. Natl. Acad. Sci. U.S.A. |
| 1356 | 100, 1535-1440. 10.1073/pnas.0437845100. |
| 1357 | |
| 1358 | Matsuda, D., and Mauro, V.P. (2014). Base pairing between hepatitis C virus RNA and 18S rRNA is required for |
| 1359 | IRES-dependent translation initiation in vivo. Proc. Natl. Acad. Sci. U.S.A. 111, 15385-15389. |
| 1360 | <u>10.1073/pnas.1413472111</u> . |
| 1361 | |
| 1362 | Morin, A., Eisenbraun, B., Key, J., Sanschagrin, P.C., Timony, M.A., Ottaviano, M. and Sliz, P., (2013). Cutting edges |
| 1363 | Collaboration gets the most out of software. Elife. 2, e01456. 10.7554/eLife.01456. |
| 1364 | |
| 1365 | Nag, N., Lin, K.Y., Edmonds, K.A., Yu, J., Nadkarni, D., Marintcheva, B., and Marintchev, A. (2016). eIF1A/eIF5B |
| 1366 | interaction network and its functions in translation initiation complex assembly and remodeling. Nucleic Acids Res. |
| 1367 | 44, 7441-7456. 10.1093/nar/gkw552. |
| 1368 | |
| 1369 | Neupane R, Pisareva VP, Rodriguez CF, Pisarev AV, Fernández IS. (2020) A complex IRES at the 5'-UTR of a viral |
| 1370 | mRNA assembles a functional 48S complex via an uAUG intermediate. Elife. 9, e54575. 10.7554/eLife.54575. |
| 1371 | |
| 1372 | Odreman-Macchioli, F., Baralle, F.E., and Buratti, E. (2001). Mutational analysis of the different bulge regions of |
| 1373 | hepatitis C virus domain II and their influence on internal ribosome entry site translational ability. J Biol Chem. 276, |
| 1374 | 41648-41655. 10.1074/jbc.M104128200. |
| 1375 | |
| 1376 | Passmore, L.A., and Russo, C.J. (2016). Specimen Preparation for High-Resolution Cryo-EM. Methods Enzymol. |
| 1377 | 579, 51-86. 10.1016/bs.mie.2016.04.011. |
| 1378 | |
| 1379 | Passmore, L.A., Schmeing, T.M., Maag, D., Applefield, D.J., Acker, M.G., Algire, M.A., Lorsch, J.R., and |
| 1380 | Ramakrishnan, V. (2007). The eukaryotic translation initiation factors eIF1 and eIF1A induce an open conformation |
| 1381 | of the 40S ribosome. Mol. Cell 26, 41-50. 10.1016/j.molcel.2007.03.018. |
| 1382 | |
| 1383 | Pestova, T.V., and Hellen, C.U. (2001). Preparation and activity of synthetic unmodified mammalian tRNAi(Met) in |
| 1384 | initiation of translation in vitro. RNA 7, 1496-1505. 10.1017/s135583820101038x. |
| 1385 | |
| 1386 | Pestova, T.V., and Kolupaeva, V.G. (2002). The roles of individual eukaryotic translation initiation factors in |
| 1387 | ribosomal scanning and initiation codon selection. Genes Dev. 16, 2906-2922. 10.1101/gad.1020902. |
| 1388 | |
| 1389 | Pestova, T.V., Borukhov, S.I., and Hellen, C.U. (1998a). Eukaryotic ribosomes require initiation factors 1 and 1A to |
| 1390 | locate initiation codons. Nature 394, 854-859. 10.1038/29703. |
| | |

| 1391 | |
|------|--|
| 1392 | Pestova, T.V., Shatsky, I.N., Fletcher, S.P., Jackson, R.J., and Hellen, C.U. (1998b). A prokaryotic-like mode of |
| 1393 | cytoplasmic eukaryotic ribosome binding to the initiation codon during internal translation initiation of hepatitis C |
| 1394 | and classical swine fever virus RNAs. Genes Dev. 12, 67-83. 10.1101/gad.12.1.67. |
| 1395 | |
| 1396 | Pestova, T.V., Lomakin, I.B., Lee, J.H., Choi, S.K., Dever, T.E., and Hellen, C.U. (2000). The joining of ribosomal |
| 1397 | subunits in eukaryotes requires eIF5B. Nature 403, 332-335. 10.1038/35002118. |
| 1398 | |
| 1399 | Pestova, T.V., de Breyne, S., Pisarev, A.V., Abaeva, I.S., and Hellen, C.U. (2008). eIF2-dependent and eIF2- |
| 1400 | independent modes of initiation on the CSFV IRES: a common role of domain II. EMBO J. 27, 1060-1072. |
| 1401 | 10.1038/emboj.2008.49. |
| 1402 | |
| 1403 | Pettersen, E.F., Goddard, T.D., Huang, C.C., Couch, G.S., Greenblatt, D.M., Meng, E.C., and Ferrin, T.E. (2004). |
| 1404 | UCSF Chimeraa visualization system for exploratory research and analysis. J. Comput. Chem. 25, 1605-12. |
| 1405 | 10.1002/jcc.20084. |
| 1406 | |
| 1407 | Pisarev, A.V., Kolupaeva, V.G., Pisareva, V.P., Merrick, W.C., Hellen, C.U., and Pestova, T.V. (2006). Specific |
| 1408 | functional interactions of nucleotides at key -3 and +4 positions flanking the initiation codon with components of the |
| 1409 | mammalian 48S translation initiation complex. Genes Dev. 20, 624-36. 10.1101/gad.1397906 |
| 1410 | |
| 1411 | Pisarev, A.V., Unbehaun, A., Hellen, C.U., and Pestova, T.V. (2007). Assembly and analysis of eukaryotic translation |
| 1412 | initiation complexes. Methods Enzymol. 430, 147-77. 10.1016/S0076-6879(07)30007-4. |
| 1413 | |
| 1414 | Pisareva, V.P., Pisarev, A.V., and Fernández, I.S. (2018). Dual tRNA mimicry in the cricket paralysis virus IRES |
| 1415 | uncovers an unexpected similarity with the hepatitis C virus IRES. Elife 7, e34062. 10.7554/eLife.34062. |
| 1416 | |
| 1417 | Potter, C.S., Chu, H., Frey, B., Green, C., Kisseberth, N., Madden, T.J., Miller, K.L., Nahrstedt, K., Pulokas, J., |
| 1418 | Reilein, A., Tcheng, D., Weber, D., and Carragher, B. (1999). Leginon: a system for fully automated acquisition of |
| 1419 | 1000 electron micrographs a day. Ultramicroscopy 77, 153-161. 10.1016/s0304-3991(99)00043-1. |
| 1420 | |
| 1421 | Prince, J.B., Taylor, B.H., Rhurlow, D.L., Ofengand, J., and Zimmermann, R.A. (1982). Covalent crosslinking of |
| 1422 | tRNA1 ^{Val} to 16S RNA at the ribosomal P site: identification of crosslinked residues. Proc. Natl. Acad. Sci. U.S.A. 79, |
| 1423 | 5450-5454. 10.1073/pnas.79.18.5450. |
| 1424 | |
| 1425 | Quade, N., Boehringer, D., Leibundgut, M., van den Heuvel, J., and Ban, N. (2015). Cryo-EM structure of Hepatitis |
| 1426 | C virus IRES bound to the human ribosome at 3.9-Å resolution. Nat. Commun. 6, 7646. 10.1038/ncomms8646. |
| 1427 | |

46

- 1428 Reibarkh, M., Yamamoto, Y., Singh, C.R., del Rio, F., Fahmy, A., Lee, B., Luna, R.E., Ii, M., Wagner, G., and Asano,
- 1429 K. (2008). Eukaryotic initiation factor (eIF) 1 carries two distinct eIF5-binding faces important for multifactor
- 1430 assembly and AUG selection. J. Biol. Chem. 283, 1094-1103. <u>10.1074/jbc.M708155200</u>.
- 1431
- 1432 Reynolds, J.E., Kaminski, A., Carroll, A.R., Clarke, B.E., Rowlands, D.J., and Jackson, R.J. (1996). Internal initiation
- of translation of hepatitis C virus RNA: the ribosome entry site is at the authentic initiation codon. RNA 2, 867-878.
- Rohou, A., and Grigorieff, N. (2015). CTFFIND4: Fast and accurate defocus estimation from electron micrographs.
- 1436 J. Struct. Biol. 192, 216-221. 10.1016/j.jsb.2015.08.008.
- 1437
- Rosenthal, P.B., and Henderson, R., (2003). Optimal determination of particle orientation, absolute hand, and contrast
 loss in single-particle electron cryomicroscopy. J. Mol. Biol. 333, 721-745. 10.1016/j.jmb.2003.07.013.
- 1440
- 1441 Scheres, S.H. (2012). RELION: implementation of a Bayesian approach to cryo-EM structure determination. J. Struct.
- 1442 Biol. 180, 519-530. <u>10.1016/j.jsb.2012.09.006</u>.
- 1443
- Scheres, S.H. (2016). Processing of structurally heterogeneous cryo-EM data in RELION. Methods. Enzymol. 579,
 125-157. 10.1016/bs.mie.2016.04.012
- 1446
- Schrödinger, L.L.C. (2015). The PyMOL Molecular Graphics System, Version 2.4.1 (Shrodinger LLC).
 <u>https://pymol.org/</u>
- 1449

Simonetti, A., Brito Querido, J., Myasnikov, A.G., Mancera-Martinez, E., Renaud, A., Kuhn, L., and Hashem Y.
(2016). eIF3 Peripheral Subunits Rearrangement after mRNA Binding and Start-Codon Recognition. Mol. Cell 63,

- 1452 206-217. 10.1016/j.molcel.2016.05.033.
- 1453
- Simonetti, A., Guca, E., Bochler, A., Kuhn, L., and Hashem, Y. (2020). Structural insights into the mammalian latestage initiation complexes. Cell Rep. 31, 107497. 10.1016/j.celrep.2020.03.061
- 1456
- Sizova, D.V., Kolupaeva, V.G., Pestova, T.V., Shatsky, I.N., and Hellen, C.U. (1998). Specific interaction of
 eukaryotic translation initiation factor 3 with the 5' nontranslated regions of hepatitis C virus and classical swine fever
 virus RNAs, J. Virol. 72, 4775-4782. 10.1128/JVI.72.6.4775-4782.1998.
- 1460
- Spahn, C.M., Kieft, J.S., Grassucci, R.A., Penczek, P.A., Zhou, K., Doudna, J.A., and Frank, J. (2001). Hepatitis C
 virus IRES RNA-induced changes in the conformation of the 40s ribosomal subunit. Science 291, 19591962. 10.1126/science.1058409.
- 1464

Suloway, C., Pulokas, J., Fellmann, D., Cheng, A., Guerra, F., Quispe, J., Stagg, S., Potter, C.S., and Carragher, B.
(2005). Automated molecular microscopy: the new Leginon system. J. Struct. Biol. 151, 41-60.
10.1016/j.jsb.2005.03.010.

1468

1469 Tang, S., Collier, A.J., and Elliott, R.M. (1999). Alterations to both primary and predicted secondary structure of stem-

1470 loop IIIc of the hepatitis C virus 1b 5' untranslated region 5'UTR) lead to mutants severely defective in translation

- which cannot be complemented in trans by the wild-type 5'UTR sequence. J. Virol. 73, 2359-2364.
 10.1128/JVI.73.3.2359-2364.1999.
- 1473
- Terenin, I.M., Dmitriev, S.E., Andreev, D.E., and Shatsky, I.N. (2008). Eukaryotic translation initiation machinery
 can operate in a bacterial-like mode without eIF2. Nat. Struct. Mol. Biol. 15, 836-841. 10.1038/nsmb.1445.
- 1476
- Thakur, A., Gaikwad, S., Vijjamarri, A.K., and Hinnebusch, A.G. (2020). eIF2α interactions with mRNA control
 accurate start codon selection by the translation preinitiation complex. Nucleic Acids Res. 48, 810280-10296.
 10.1093/nar/gkaa761.
- 1480
- Tivol, W.F., Briegel, A., and Jensen, G.J. (2008). An improved cryogen for plunge freezing. Microsc. Microanal. 14,
 375-379. 10.1017/S1431927608080781.
- 1483

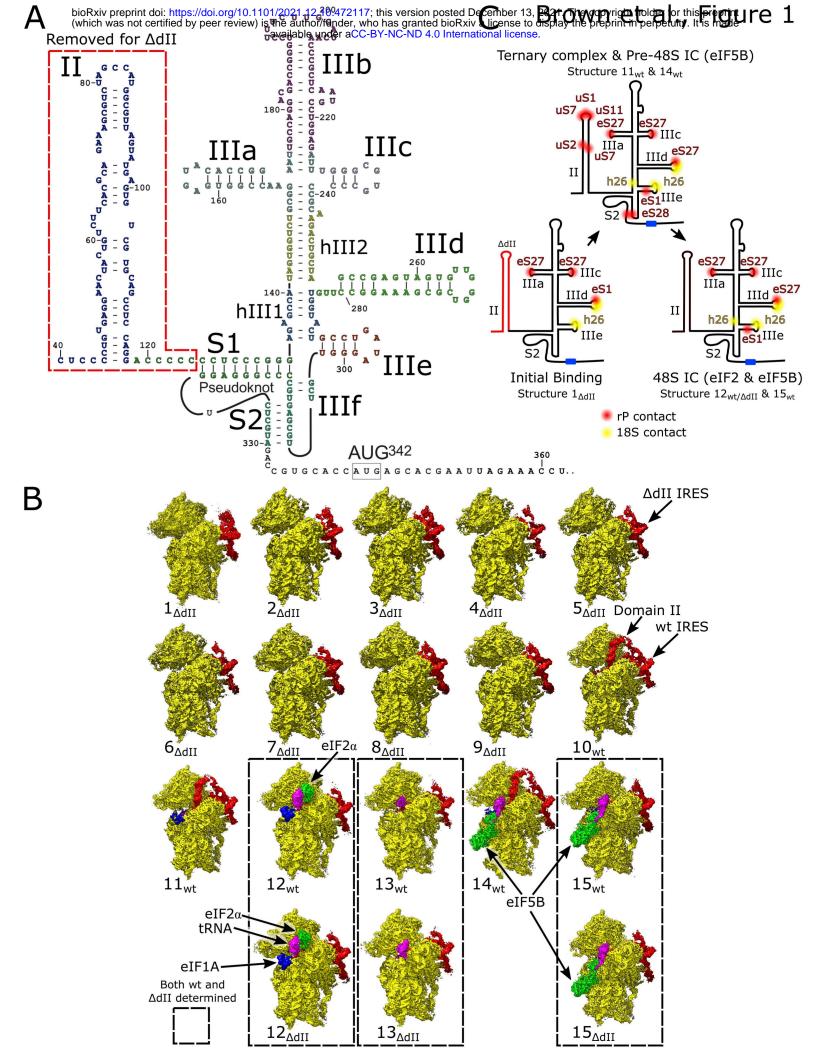
Unbehaun, A., Borukhov, S.I., Hellen, C.U., and Pestova, T.V. (2004). Release of initiation factors from 48S
complexes during ribosomal subunit joining and the link between establishment of codon-anticodon base-pairing and
hydrolysis of eIF2-bound GTP. Genes Dev. 18, 3078-3093. 10.1101/gad.1255704.

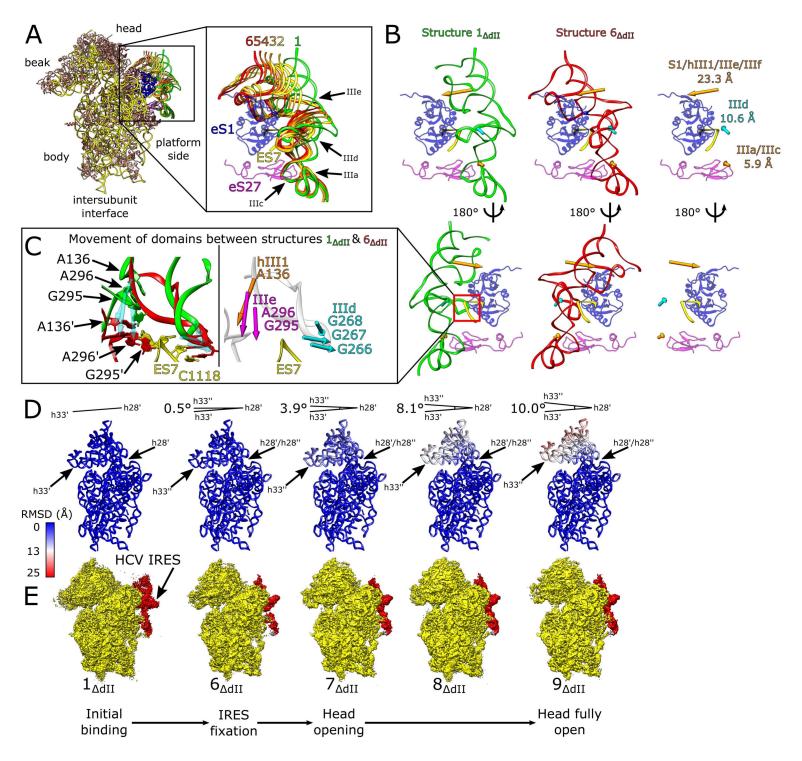
- 1487
- Wang, J., Wang, J., Shin, B.S., Kim, J.R., Dever, T.E., Puglisi, J.D., and Fernández, I.S. (2020). Structural basis for
 the transition from translation initiation to elongation by an 80S-eIF5B complex. Nat. Commun. 11, 5003.
 10.1038/s41467-020-18829-3.
- 1491

Yamamoto, H., Unbehaun, A., Loerke, J., Behrmann, E., Collier, M., Bürger, J., Mielke, T., and Spahn, C.M. (2014).
Structure of the mammalian 80S initiation complex with initiation factor 5B on HCV-IRES RNA. Nat. Struct. Mol.
Biol. 21, 721-727. 10.1038/nsmb.2859.

- 1495
- Yamamoto, H., Collier, M., Loerke, J., Ismer, J., Schmidt, A., Hilal, T., Sprink, T., Yamamoto, K., Mielke, T., Bürger,
 J., Shaikh, T.R., Dabrowski, M., Hildebrand, P.W., Scheerer, P., and Spahn, C.M. (2015). Molecular architecture of
 the ribosome-bound Hepatitis C Virus internal ribosomal entry site RNA. EMBO J. 34, 3042-3058.
 10.15252/embj.201592469.
- 1500

- 1501 Yokoyama, T., Machida, K., Iwasaki, W., Shigeta, T., Nishimoto, M., Takahashi, M., Sakamoto, A., Yonemochi, M.,
- Harada, Y., Shigematsu, H., Shirouzu, M., Tadakuma, H., Imataka, H., and Ito, T. (2019). HCV IRES captures an
 actively translating 80S ribosome. Mol. Cell 74, 1205-1214.e8. 10.1016/j.molcel.2019.04.022.
- 1504
- 1505 Zheng, A., Yu, J., Yamamoto, R., Ose, T., Tanaka, I., and Yao, M. (2014). X-ray structures of eIF5B and the eIF5B-
- 1506 eIF1A complex: the conformational flexibility of eIF5B is restricted on the ribosome by interaction with eIF1A. Acta
- 1507 Crystallogr. D Biol. Crystallogr. 70, 3090-3098. 10.1107/S1399004714021476.
- 1508
- Zheng, S.Q., Palovcak, E., Armache, J.P., Verba, K.A., Cheng, Y., and Agard, D.A. (2017). MotionCor2: anisotropic
 correction of beam-induced motion for improved cryo-electron microscopy. Nat. Methods 14, 331-332.
 10.1038/nmeth.4193.
- 1512
- Zivanov, J., Nakane, T., Forsbery, B.O., Kimanius, D., Hagen, W.J., Lindahl, E. and Scheres, S.H.W. (2018). New
 tools for automated high-resolution cryo-EM structure determination in RELION-3. Elife 7, e42166.
 10.7554/eLife.42166
- 1516
- 1517 Zivanov, J., Nakane, T., and Scheres, S.H.W. (2019). A Bayesian approach to beam-induced motion correction in
- 1518 cryo-EM single-particle analysis. IUCr. J. 6, 5-17. 10.1107/S205225251801463X
- 1519





bioRxiv preprint doi: https://doi.org/10.1101/2021.12.10.472117; this version posted December 13, Par chevepyrige folder for this preprint in perpetuity. It is made a valiable under a CC-BY-NC-ND 4.0 International license.

